Title
LiDAR-derived topography and forest structure predict fine-scale variation in daily surface temperatures in oak savanna and conifer forest landscapes

Authors
Davis, Frank W
Synes, Nicholas W
Fricker, Geoffrey A
et al.

Publication Date
2019-05-01

DOI
10.1016/j.agrformet.2019.02.015

LiDAR-derived topography and forest structure predict fine-scale variation in daily surface temperatures in oak savanna and conifer forest landscapes

Authors

Frank W. Davis[a*], Nicholas W. Synes[b], Geoffrey A. Fricker[b,c,d], Ian M. McCullough[e], Josep M. Serra-Diaz[f, g], Janet Franklin[b,d], and Alan L. Flint[h]

Affiliations

[a] Bren School of Environmental Science & Management, University of California, Santa Barbara, CA 93106, USA

[b] School of Geographical Sciences & Urban Planning, Arizona State University, P.O. Box 875302, Tempe, AZ 85287-5302, USA

[c] Social Sciences Department, California Polytechnic University, San Luis Obispo, San Luis Obispo, CA 93407, USA

[d] Department of Botany and Plant Sciences, University of California, Riverside, Riverside, California. Riverside, CA 92507, USA

[e] Department of Fisheries and Wildlife, Michigan State University, East Lansing MI, 48824 USA

[f] Université de Lorraine, AgroParisTech, Inra, Silva, 54000 Nancy, France

[g] Center for Biodiversity Dynamics in a Changing World (BIOCHANGE), Department of Bioscience, Aarhus University, Denmark

[h] California Water Science Center, USGS, 6000 J Street, Sacramento, California 95819 USA

* Corresponding author. Email address: fwd@bren.ucsb.edu

ABSTRACT

In mountain landscapes, surface temperatures vary over short distances due to interacting influences of topography and overstory vegetation on local energy and water balances. At two study landscapes in the Sierra Nevada of California, characterized by foothill oak savanna at 276-481 m elevation and montane conifer forest at 1977-2135 m, we deployed 288 near-surface (5 cm above the surface) temperature sensors to sample site-scale (30 m) temperature variation related to hillslope orientation and vegetation structure and microsite-scale (2-10 m) variation related to microtopography and tree overstory. Daily near-surface maximum and minimum temperatures for the 2013 calendar year were related to topographic factors and vegetation overstory characterized using small footprint LiDAR imagery acquired by the National Ecological Observatory Network (NEON) Airborne Observation Platform (AOP). At both landscapes we recorded large site and microsite spatial variation in daily maximum temperatures, and less absolute variation in daily minimum temperatures. Generalized boosted regression trees were estimated to measure the influence of tree canopy density, understory solar radiation, cold-air drainage and pooling, ground cover and microtopography on daily maximum and minimum temperatures at site and microsite scales. Site-scale models based on indices of understory solar radiation and landscape position explained an average of 61-65% of daily variation in maximum temperature; site-scale models based on tree canopy density and landscape position explained 65-83% of variation in minimum temperatures. Models explained <15% of variation in microsite-scale maximum temperatures but within-site heterogeneity was significantly correlated with within-site heterogeneity in modeled understory radiation at both landscapes. Tree canopy density and slope explained 33% of microsite-scale variation in minimum temperatures at savanna sites. Our results demonstrate that it is feasible to model site-scale variation in daily surface temperature extremes and within-site heterogeneity in surface temperatures using LiDAR-derived variables, supporting efforts to understand cross-scale relationships between surface microclimates and regional climate change. Improved understanding of topographic and vegetative buffering of thermal microclimates across mountain landscapes is key to projecting microclimate heterogeneity and potential species' range dynamics under future climate change.

KEYWORDS**:** microclimate, insolation, cold-air drainage, NEON

Highlights

- Spatial variation in daily maximum surface temperatures is high in foothill oak savannas and even higher in montane conifer forest landscapes
- Modeled understory radiation, landscape position and tree canopy explain >60% of observed variation in daily surface temperature extremes
- Topographic and canopy controls on surface temperature extremes vary seasonally
- NEON LiDAR data are useful for modeling site and microsite variation in surface temperatures

Abbreviations

Acronym	**Term**	**units**
AOP	NEON Airborne Observation Platform, which collects remote sensing data over NEON field sites.	
CAP	Cold-air pooling index (Eq. 5)	m
CD	Tree canopy density, the percent of ground covered by tree canopy (0-100) in a circle of specified radius centered on the point (Eq. 1)	%
CDs	Tree canopy density within a semi-circle of specified radius south of the temperature sensor	%
DEM	Digital elevation model.	m
GCs	Fractional ground cover (shrubs, large herbs and large woody debris) in a semicircle of specified radius south of the point.	%
LAI	Leaf Area Index	m^2/m^2
LiDAR	Light Detection and Ranging	
LPI	Laser Penetration Index, derived from LiDAR (Eq. 2)	0-1
NEON	National Ecological Observatory Network	
S	Slope calculated from DEM	deg
SJER	San Joaquin Experimental Range	
SR	Modeled integrated daily solar radiation	Whm^{-2}
TEF	Teakettle Experimental Forest	
TPI	Topographic Position Index, a proxy for cold-air drainage and pooling (Eq. 4)	m
UR	Index of understory direct solar radiation (Eq. 3)	WHm^{-2}

1. Introduction

Climate varies continuously across spatial scales ranging from macroclimates (>2 x 10^5 m horizontally) to mesoclimates (10^3 – 2 x10^5 m), local topoclimates (10^2-10^4 m), and ultimately microclimates (10^{-1} - 10^2 m) (Barry, 1970; Geiger et al., 2009). Microclimatic variation within a few decimeters of the ground surface is of particular interest to ecologists and natural resource managers because this is the climate that many organisms experience (Kearney and Porter, 2009; Rosenberg et al., 1983). To better understand how species could be affected by ongoing climate change, ecologists have intensified research to characterize spatial variation in near-surface temperature regimes at topoclimate and microclimate scales (e.g., Ashcroft and Gollan, 2013a; Lenoir et al., 2017; Scherrer and Körner, 2011). Attention has focused on the potential for thermal refugia in mountain landscapes, which harbor large topographic variation in surface temperatures at topoclimate and microclimate scales (Ashcroft and Gollan, 2013b; Dobrowski, 2011). This fine-scale heterogeneity has important ramifications in moderating climate change exposure for species and communities (Hannah et al., 2014; Woods et al., 2015).

Overstory trees and shrubs are another important source of surface temperature variation. Numerous studies have documented large meter-to-meter differences in daily surface temperature extremes between understories compared to edges or open areas in temperate forests (reviewed by Chen et al., 1999; Schmidt et al., 2017), semi-arid woodlands and savannas (Belsky et al., 1993; Breshears et al., 1998; Parker and Muller, 1982) and shrublands (Pierson and Wight, 1991). Differences in daytime temperatures are mainly due to overstory interception of incident shortwave solar radiation and effects of vegetation on near-surface air movement and sensible heat exchange, whereas nighttime differences are largely due to canopy absorption and re-radiation of longwave radiation emitted by the ground surface (Geiger et al., 2009). Fine-scale spatial heterogeneity in surface temperatures is especially pronounced under discontinuous tree and shrub cover depending on canopy arrangement, height and closure (Breshears, 2006; Martens et al., 2000). Heterogeneity can be extreme in semi-arid ecosystems where high summer insolation and dry surface soils combine to produce high surface temperatures in open areas (Belsky et al., 1993; Parker and Muller, 1982).

In mountainous terrain the influence of overstory vegetation on surface temperatures is complicated by spatial variation in surface energy balance with changing elevation, slope orientation (Musselman et al., 2013), terrain shadowing (Flint and Childs, 1987), air flow patterns and cold-air pooling (Burns and Chemel, 2014; Lundquist et al., 2008), hillslope hydrology, snowpack depth and duration (Broxton et al., 2015), as well as the co-variation of vegetation structure with topographic position (Ford et al., 2013). Understanding the joint influence of vegetation and terrain on fine-scale variation in surface temperature extremes is important both in assessing the potential for climate buffering in mountainous areas and in weighing vegetation management options that favor biodiversity persistence (Frey et al., 2016).

Small-footprint Light Detection and Ranging (LiDAR) imaging systems now provide unprecedented ability to characterize surface topography and overlying vegetation structure at very fine scales over large areas (Eitel et al., 2016), enabling cross-scale study of biophysical controls on solar radiation and associated surface temperature regimes in mountainous regions (Bode et al., 2014; Frey et al., 2016; Lenoir et al., 2017; Musselman et al., 2013). From 2011-2017 we deployed temperature microsensors to monitor near-surface air temperatures in a foothill oak savanna landscape and a montane conifer forest landscape in the southern Sierra Nevada, California. We are studying these landscapes as part of a larger effort to relate microclimates to tree seedling establishment in California (Davis et al., 2016; Dingman et al., 2013; Serra-Diaz et al., 2016). In this paper we analyze daily maximum and minimum surface temperatures for 2013 in relation to topography and overstory vegetation as characterized by discrete return, small-footprint LIDAR data acquired in that year by the NEON AOP (Kampe et al., 2010).

Our objectives here are to:

1) Evaluate the magnitude and spatiotemporal patterns of local topoclimatic and microclimatic variation in daily surface temperature extremes across Mediterranean-climate savanna and forest landscapes.

    - Based on physical theory and prior empirical research we expected greater heterogeneity in maximum than minimum surface temperatures at both topoclimate and microclimate scales (Ashcroft and Gollan, 2013b);

2) Quantify the dynamic influence of topography and overstory vegetation on surface temperatures at both topoclimate and microclimate scales as a function of time of year.

- We expected to observe a larger influence of topography on solar radiation and surface temperatures in areas with steeper slopes (Dubayah et al., 1990). We also expected topography to influence cold-air drainage and cold-air pooling in canyons and stream valleys (Bergen, 1969; Pypker et al., 2007; Lundquist et al., 2008). We expected significant canopy buffering of surface temperature extremes at both topoclimate and microclimate scales, especially during summer months and in montane forested landscape with taller trees and higher tree cover (Breshears et al., 1998; Chen et al., 1999; Ma et al., 2010)

3) Evaluate the potential to model microclimatic variation in temperature extremes using small footprint LIDAR obtained by the NEON AOP.

- Prior research has demonstrated the potential of small footprint LiDAR to characterize microtopography and 3-dimensional vegetation structure (Musselman et al., 2013). Given NEON plans to deploy the AOP across multiple regions for many years, the present study constitutes an early test of the applicability of NEON LiDAR data products for microclimate research.

2. Methods

2.1. Study sites

The Sierra Nevada region experiences a Mediterranean-type climate with warm to hot, dry summers and cool to cold, wet winters. Our foothill savanna landscape is the San Joaquin Experimental Range (SJER; 37°5’45"N, 119°43’W, www.fs.fed.us/psw/ef/san_joaquin), a rangeland research area that also serves as the NEON core site for the Pacific Southwest region (http://www.neonscience.org/field-sites/field-sites-map/SJER) (Fig. 1, 2). Our measurements were from a ~24 km^2 area spanning 276-481 m in elevation with average slope of 8°. Mean monthly temperatures in winter have historically ranged from 4-10 °C and summer monthly mean temperatures from 24-27 °C (https://www.fs.fed.us/psw/ef/san_joaquin/). Most precipitation falls as rain between December and March, averaging around 490 mm annually. The area supports savanna and open woodland dominated by winter-deciduous blue oak (*Quercus douglasii*), evergreen interior live oak (*Q. wislizenii*), and evergreen foothill pine (*Pinus sabiniana*). Oaks are generally 6-10 m in height. The herb layer, which is grazed by cattle, is 0.1-1 m in height and dominated by Mediterranean annual grasses that senesce by May, notably *Bromus hordeaceous*, *B. diandrus*, and *Avena fatua*.

[Fig. 1 about here]

Our montane forest study landscape is within the Teakettle Experimental Forest (TEF; 36°58'N, 119°1'W, http://www.fs.fed.us/psw/ef/teakettle), 53 km southeast of SJER (Fig. 1, 2). Our samples span a ~4 km^2 area and range from 1977-2135 m elevations. Based on 10 m digital elevation data, slopes across TEF average 24°. Intensive ecological and microclimate research has been conducted here over the past 20 years (Ma et al., 2010; North et al., 2010), and TEF is also one of two re-locatable NEON sites for the Pacific Southwest region. Mean monthly summer temperatures range from 14-18 °C, winter temperatures from 0-2 °C. Mean annual precipitation is ~1200 mm, falling mainly as snow between November and April. Old-growth mixed-conifer forest ranges from open stands with isolated tree crowns to closed forest, and the landscape also contains persistent forest gaps averaging 5-20 m in diameter (Ma et al., 2010). Open areas are predominantly shrub covered, duff or rock outcroppings. The forest is dominated by evergreen conifers; white fir (*Abies concolor*), red fir (*A. magnifica*), sugar pine (*Pinus lambertiana*) and Jeffrey pine (*P. jeffreyi*) are among the largest diameter and tallest trees, with heights of 40 - >60 m. Shrub cover consists primarily of whitethorn ceanothus (*Ceanothus cordulatus*) and green leaf manzanita (*Arctostaphylos patula*) (North et al., 2010).

[Fig. 2 about here]

2.2. Temperature data

One hundred and thirty-three temperature sensors were located at 18 sites across SJER; 141 sensors were placed at 24 sites across TEF. Sites were chosen to sample topographic variation in surface temperature within a narrow range of elevations on northeast to southwest-facing slopes, ridges and valleys (Fig. 3). For the rest of the paper we refer to this sample of sites across the landscape as the "site scale" aimed at capturing topoclimatic effects related to landscape position and hillslope orientation.

To characterize surface temperature variation within a site, 21 sensors were arranged in an identical pattern around and in six, 5x5 m experimental gardens (Fig. 4). We refer to these densely instrumented sites as “arrays” and within-array variation as "microsite scale” variation. The gardens were used for seedling establishment trials (Davis et al., 2016) and were located to sample microsite variation on generally north-facing, south-facing and level sites in the same local area of the landscape (Fig. 3). Gardens were deliberately located in canopy gaps at least 8-m wide, but the sensors in the surrounding arrays could be in gaps, tree understories, in or near shrub patches, and on various microtopographic positions. The location of each temperature sensor was collected using a differential global positioning system that provided sub-meter accuracy for the majority of sensors and sub-2 m accuracy in all cases.

Temperatures were recorded using HOBO© (Onset, www.onsetcomp.com) model U23-004 sensors, which have an operating range of -40° to 70 °C and accuracy of ±0.21 °C from 0° to 50 °C. Sensor integrity was checked for 24 h in a constant-temperature environment prior to field deployment. Sensors were suspended 5 cm above the soil surface and shielded from direct sunlight by inverted white styrene funnels 10 cm in diameter. For brevity we refer to these near-surface air temperatures as "surface temperatures" but emphasize that these were not taken on the ground surface. Temperatures were recorded at 10-min intervals. Data were downloaded manually twice over the course of the year and underwent extensive automated and manual quality control prior to the derivation of summary variables, resulting in a relatively conservative selection of daily values for the 2013 calendar year (Table A.1). Pre-processed and processed data can be downloaded from the Environmental Data Initiative (https://environmentaldatainitiative.org/).

2.3. LiDAR Data

The NEON AOP simultaneously collects airborne LiDAR, hyperspectral and three-band color orthophotography datasets timed to be as close to the period of regional ‘peak vegetation greenness’ as practicable. In 2013, NEON AOP datasets were collected for SJER between June 9th and 13th and for TEF between June 14th and 15th (Kampe et al., 2013). This was close to peak greenness for TEF, but late for April-May peak greenness at SJER.

The 2013 NEON campaign at SJER and TEF is described in detail by Kampe et al. (2013). The LiDAR point cloud data have high ground locational precision (<0.1 pixel), vertical sampling precision of 0.3 m, and resolution ranging from 1.7 to 3.8 points m^{-2} at TEF and SJER, respectively. We did not conduct an independent test of the accuracy of the NEON Level 1 LiDAR point cloud data. The data products were released as engineering-grade, that is, produced using NEON-generated algorithms that are the preliminary versions of those that will be used for science-grade data products (Kampe et al., 2013).

2.4. Elevation and slope

NEON AOP Level 1 LiDAR data were reprocessed from calibrated point cloud data to create a 1-m resolution digital elevation model (DEM). The procedure discriminated ground vs. non-ground points and censored points that fell either below the immediate ground surface or that exceeded 80 m above the ground surface. We manually edited the point cloud classification to remove additional topographic outliers and anomalies. From the classified and edited point cloud, a 1-m resolution triangulated ‘last-return’ surface was rasterized to produce a DEM that was resampled to 2-m resolution to match the locational accuracy of the temperature sensors. Slope angle (S) was derived from the 2 m DEM using the ‘Slope’ tool in ArcGIS 10.4.

2.5. Solar radiation

The sum of direct and diffuse solar irradiance at each sensor location was calculated on a 30-minute time step and summed to calculate daily solar radiation using the ‘Points Solar Radiation’ modeling tool in ArcGIS 10.4 (Fu and Rich, 2002). Daily atmospheric transmittance values were estimated as the ratio of ground to top-of-atmosphere solar radiation, where ground radiation data (300 to 2800 nm) were obtained from flux towers maintained by the Southern Sierra Critical Zone Observatory for SJER (Goulden and Kelley, 2016) and the P301 Tower near TEF (37°04'N, 119°12'W, 2030 m elevation) (Goulden and Kelley, 2015). Microsite-scale daily incident solar radiation was modeled at 2-m resolution (*SR2*); site-scale daily incident solar radiation was modeled at 30-m resolution (*SR30*).

2.6. Tree Canopy Density, Laser Penetration Index, and Ground Cover

LiDAR point returns were separated into ground surface returns, ground cover returns (<1 m above the putative ground surface), and tree overstory returns (> 1 m above the putative ground surface). The 1 m threshold for tree overstory returns follows Musselman et al. (2013). Tree canopy density (*CD*) was calculated using the 'Las Tools' toolkit (https://rapidlasso.com) as:

$$CD = [1 - (GR + GC) / TR] * 100 \quad (1)$$

where *CD* is the percent of the ground covered by tree canopy, *TR* is the total number of return points, *GR* is the number of ground returns, and *GC* the number of ground cover returns on a 1 m grid, subsequently resampled to 2 m resolution. Site-scale canopy density (*CD30*) was calculated as mean *CD* within a 30-m radius centered on each sensor location or, in the case of sensor arrays, on the center of the array. We also calculated *CD* at 60 m and 90 m scales but model results were either comparable or inferior to those using *CD30*, so only results for *CD30* are presented here. For microsite-scale analyses *CD* was calculated within circles of 2.5, 5, and 10 m radii (*CD2.5*, *CD5*, *CD10*).

The Laser Penetration Index (LPI) is the fraction of LiDAR point returns that reaches the understory:

$$LPI = (GR + GC) / TR \quad (2)$$

where LPI is unitless and ranges from 0 to 1. To model sunlight penetration through the forest canopy, we calculated *LPI* for a semi-circle south of the sensor (*LPIs*) with a radius of 30 m for site-scale analysis (*LPI30s*) and 10m for microsite-scale analysis (*LPI10s*).

For modeling daily maximum temperatures, we calculated a simple proxy for understory irradiance as:

$$UR = SR * LPIs \quad (3)$$

where *UR* is total daily understory irradiance in Whm^{-2}. This proxy for actual understory incoming shortwave radiation does not separate direct from diffuse terms (see Bode et al. 2014), does not account for partial transmission of sunlight through the tree canopies or variation in path length through the tree canopy as a function of sun position, and ignores canopy interception of incoming direct beam radiation from the northeast and southwest quadrants during early morning and late afternoon hours between the Spring and Autumnal equinoxes.

2.7. Cold-air drainage and pooling

Previous studies in the Sierra Nevada, including TEF, have documented lower temperatures and greater snow persistence in riparian areas and local topographic depressions subject to the influences of cold-air drainage and cold-air pooling (Curtis et al., 2014; Lundquist et al., 2008; Rambo and North, 2009). We tested two topographic indices that have been developed to predict locations prone to cold-air drainage or cold-air pooling effects at landscape-to-regional scales. The cold-air pooling index of Lundquist et al. (2008) analyzes a DEM to locate flat valley bottoms and concave areas where cold-air pools are likely to form (Curtis et al. 2014). The algorithm relies on a Topographic Position Index (*TPI*) – the difference between a location's elevation and the mean elevation in a circle surrounding the point that approximates the typical peak-to-peak or ridge-to-ridge distance:

$$TPI \ = z - \overline{z(d)} \quad (4)$$

where TPI is a location's relative topographic position in meters, z is the elevation of the location, and $\overline{z(d)}$ is the mean elevation in a circle with radius d surrounding the point. Ashcroft and Gollan (2013b) developed a similar index using the difference between a location's elevation and the minimum elevation in a circle of 500-m radius, taking the log of this distance as an index of cold-air pooling potential:

$$CAP = \log(z - \min(z(d))) \quad (5)$$

where *CAP* is the cold-air potential in meters, z is the elevation of the location, and min(z(d)) is the minimum elevation within *d* meters of the location. Both *TPI* and *CAP* are scale-dependent and sensitive to extent of the circular neighborhood used to calculate relative elevation. To test these measures at different spatial scales we calculated both indices based on neighborhood radii of 150, 250, 500 and 1000 m (*TPI[150-1000],CAP[150-1000]*).

2.8. Statistical Analyses

Temperature micro-sensors such as those used in this study measure temperature variation on the scale of cm and are highly sensitive to small differences in placement and radiation shield design (Ashcroft and Gollan, 2013b; Geiger et al., 2009; Graae et al., 2012; Holden et al., 2013). Both absolute and relative temperatures will be affected by factors such as sensor height, weather conditions and shielding. Maximum surface temperatures may be especially sensitive to shield design (Holden et al., 2013). We focus here on relative differences as indicative results, although we expect differences will be larger in locations with more hot, sunny weather, or where sensors are inadvertently positioned slightly closer to the ground surface.

Data from SJER and TEF were analyzed separately to model daily *Tmax* and *Tmin* as a function of site-scale and microsite-scale biophysical variables. At TEF we limited our analysis to the period April 1 to September 30, when most or all sensors were snow-free. For SJER we analyzed the complete calendar year. Predictor variables and scales were selected based on previous research outlined in the introduction, general principles of surface energy balance, and extensive exploratory analysis with solar radiation, canopy density, understory radiation and cold-air pooling rendered across a range of spatial scales.

For the site-scale analysis we included a single sensor from each site across the landscape for each daily model. At sites with sensor arrays, we included the single sensor recording the median value for the array on that day. The resulting daily sample sizes were 21-24 for TEF and 17-18 for SJER. Given these small sample sizes we limited the number of site-scale model predictor variables to two and did not include highly correlated variables in the same model. Predictor variables tested at the site scale included those characterizing solar radiation regime (*SR30*), canopy effects (*CD30*), understory radiation (*UR30*) and cold-air drainage or pooling potential (*TPI[150-1000]*,*CAP[150-1000]*).

For microsite-scale analyses we included only array sensors and analyzed each sensor's departure from the daily mean of all sensors at that array. Microsite-scale variables included elevation (*DEM2*), slope angle from the 2-m DEM (*S2*), three scales of canopy density (*CD2.5*, *CD5*, *CD10)* and understory radiation (*UR2.5*, *UR5*, *UR10*), and solar radiation (*SR2*).

Generalized Boosted Regression Tree models were estimated using the R package 'gbm' (Ridgeway, 2007) along with the package 'caret' (Kuhn, 2017) for calibration. This ensemble statistical learning approach was selected because it is suitable for handling different types of predictor variables, and for characterizing complex data-generating processes (Elith et al., 2008; Hastie et al., 2009). Site-scale model parameters were calibrated with 10-fold cross-validation and a full factorial design with interaction depth (i.e., decision tree size) varied from 1 to 3. We explored a range of parameter settings but in the models reported here the number of tree models varied from 1,000 to 5,000 in increments of 1,000, and the shrinkage rate was kept constant at 0.001.

To simplify presentation of model results we report 2-factor models for those factors and scales that on average, based on adjusted r^2, best predict daily temperature extremes across all daily models. Given high correlations among some predictor variables and for the same factor at different scales (Tables A.2, A.3), many other models were only slightly inferior to those reported here, and could even be slightly better on specific days.

3. Results

3.1. Daily surface temperature extremes at foothill savanna and montane forest landscapes

Temperature records for the foothill and montane landscapes are summarized in Figure 5 and Table 1. Daily maximum temperatures across the foothill oak savanna landscape (SJER) routinely exceeded 50 °C in summer months and ranged widely between sites, with hottest and coolest sites differing on average by 13.1°C across the year as well as for the period April 1 through September 30 when data were available for both savanna and montane forest sites. Spatial variation in *Tmax* across the montane forest landscape was generally higher than at the foothill landscape, with daily inter-site temperature range averaging 15.6°C from April through September. Between April and September at both sites, inter-site variation in *Tmax* was lowest in June-August summer months (Table 1, Fig. A.1). In absolute terms, inter-site variation in *Tmin* was low at both oak savanna and conifer forest landscapes, although relative to daily means the standard deviation in *Tmin* was as high or higher than that for *Tmax* (Table 1).

[Fig. 5 about here]

Daily *Tmax* was consistently 5-9 °C higher on the warmest (south-facing grassland) vs. coolest (north-facing woodland) arrays at SJER (Fig. 6). Within arrays, daily standard deviations in *Tmax* were comparable to those at TEF, averaging 3.4-4.6 °C. Daily *Tmin* in SJER arrays was generally 4-5 °C lower on the coolest site (level open savanna) relative to the warmest site (rocky, southwest-facing slope) (Fig. A.2). Within-array variation in *Tmin* was low, with daily standard deviation of array means usually <1 °C.

[Table 1 about here]

At the montane landscape (TEF), daily *Tmax* was 3-7 °C higher for south and southwest-facing arrays vs. north and northeast arrays (Fig. 6). *Tmax* also varied considerably at the microsite scale within arrays, with daily standard deviations averaging 4-6 °C at five sites and a maximum of 9.7 °C at one level site. Daily *Tmin* values were typically 0.5-3 °C higher for arrays on two north-to-northeast facing slopes compared to those on south-facing and level sites (Fig. A.2). Microsite variation in minimum temperatures at TEF was low, with standard deviations of 0.2-0.5 °C within arrays.

[Fig. 6 about here]

3.2. Daily temperature models, oak savanna landscape

At SJER, site-scale variation in *Tmax* was best modeled by the understory radiation index (*UR30)* and topographic position index (*TPI250)*, which combined to explain 18-89% (mean adj. r^2 = 0.63) of variation in 365 daily models (Fig. 7). The relative influence of *UR30* averaged 60% vs. 40% for *TPI250*. Partial dependence on *UR30* averaged 2.3 °C; in other words, surface temperature at the site with highest UR30 was predicted to be, on average, 2.3 °C warmer than that at the site with lowest *UR30*. Model partial dependence on *UR30* was lowest during late February-early March and June-August when spatial variation in *Tmax* was also relatively lower (Fig. 7, Fig. A.1). The effect of *TPI250* was most pronounced in March-May, when partial dependence generally ranged from 2-6 °C, and was lowest in July through October (Fig. 7). Thus maximum daily surface temperatures at sites that were higher in the landscape (upper slopes and ridges) were predicted to be warmer than relatively low sites in valleys and riparian areas.

[Fig. 7 about here]

Site-scale models for *Tmin* across the oak savanna landscape based on canopy density *CD30* and *CAP150* explained 0.19-0.86 (mean adj. $r^2 = 0.65$) of daily site variation (Fig. 8). Relative influence of CD30 exceeded that of *CAP150* throughout the year, averaging 62%, but partial dependence varied from positive (i.e., higher canopy was associated with higher minimum daily temperatures) to negative from January through early May, was generally positive from mid-May through September, and then generally negative from October through December (Fig. 8). Partial dependence for *CAP150* ranged from 0.6-5.84 °C (mean 1.84 °C), such that sites relatively low in the landscape were modeled as experiencing consistently lower minimum daily temperatures (Fig. 8).

[Fig 8 about here]

Microsite-scale models for *Tmax* based on *UR[5,10]*, *SR2* and *GCs2.5* were generally weak at predicting intra-site maximum temperatures (mean adj. $r^2 < 0.15$). However, within-array standard deviation in *Tmax* was significantly correlated with within-array standard deviation in *UR5* ($r = 0.51$, $p < 0.001$) (Fig. A.3).

Microsite-scale models for *Tmin* based on *CD10* and slope (*S2*) explained 0.07 – 0.51 (mean adj. $r^2 = 0.33$) of the variation in *Tmin* among sensors within garden arrays (Fig. 9). Minimum temperatures increased with increasing *CD10*, with partial dependence ranging from 0-1.2 °C (average = 0.6 °C).

Tmin also increased with increasing slope angle, although the magnitude of the effect was small (average partial dependence = 0.2 °C).

[Fig. 9 about here]

3.3. Daily temperature models, montane conifer forest landscape

At TEF, general boosted models based on *UR30* and *TPI500* explained 35-94% (mean adj. r^2 = 0.63) of observed site-scale variation in daily *Tmax* (Fig. 10a). Model skill was generally higher in May and June and lower on days with highest atmospheric transmittance (Fig. A.4). The relative influence of *UR30* in daily models averaged 73% vs. 27% for *TPI500*. Partial dependence of *Tmax* on *UR30* ranged from 2 -10 °C (mean= 4.6 °C), and the association of *UR30* with *Tmax* was generally weaker in late June through August when inter-site variation in *Tmax* was also lower (Fig. 10a, Fig. A.1). Model partial dependence on *TPI500* generally ranged from -4 to 4 °C (mean= 0.9 °C) with one outlying value of 8.0 °C (Fig. 10a). From April through July, *Tmax* at the site with highest *TPI500* (i.e., highest relative elevation) was predicted to be 1.4 °C warmer on average than that with the lowest *TPI500*. The influence of *TPI500* varied considerably from August through September, when on many days sites with lower *TPI500* were relatively warmer (Fig. 10a).

[Fig. 10 about here]

General boosted models based on *CD30* and *TPI500* explained 32-95% (mean adj. r^2 = 0.83) of site-scale variation in *Tmin*, with less variation in daily model performance than for *Tmax* models (Fig. 10b). The relative influence of *CD30* averaged 74% vs. 26% for *TPI500*. Partial dependence on *CD30* ranged from -0.5-4.5 °C, and on average *Tmin* at the site with highest *CD30* was predicted to be 2.6 °C warmer than the site with lowest canopy cover. *Tmin* at the site with lowest *TPI500* was predicted to be 0.3 °C cooler on average than the highest site, although the effect of topographic position varied considerably in April, May and late September (Fig. 10b).

At the microsite scale, fitted models (not shown) had low skill in predicting *Tmax* or *Tmin*, with adjusted r^2 generally < 0.15. However, the magnitude of microsite variation (standard deviation) in

Tmax was significantly associated with microsite variation in ground cover (*GCs2.5*) ($r = 0.62$, $p < 0.001$) and *UR10* ($r = 0.51$, $p < 0.001$) (Fig. A.5).

4. Discussion

4.1. Site- and microsite-scale variation in surface temperature extremes

Our study was designed to sample inter- and intra-site variation in temperature regimes in foothill oak savanna and montane conifer forest landscapes in Mediterranean-climate California. The deployment of 133 sensors at the foothill landscape and 141 sensors at the montane landscape, with 6 densely instrumented sites in both landscapes, allowed us to investigate spatial variability at both site and microsite scales. We recorded large site-scale and microsite-scale variation in surface temperature extremes across both landscapes, particularly in maximum temperatures. Warm, dry conditions and early snowmelt in the southern Sierra Nevada in 2013 associated with regional drought (Asner et al., 2016; Robeson, 2015) produced unusually long periods of dry surface soils that probably exacerbated the role of discontinuous overstory vegetation as a source of both site- and microsite-scale spatial variation in *Tmax* (Belsky et al., 1993; Breshears et al., 1998).

Across foothill savanna sites, the standard deviation of daily maximum temperatures was typically 5-15% of the mean, with lower variation in summer and winter months and higher variation in spring and fall. Highest inter-site variation was recorded in early April, by which time the deciduous oaks were probably nearing full canopy development (Ryu et al., 2012) thereby enhancing contrast between grasslands and woodland sites (e.g., Baldocchi et al., 2004). Moreover, in April we would expect high spatial variance in midday solar irradiance and surface soil moisture as a function of local slope and aspect. Similarly, the lower spatial variation in summer surface *Tmax* is probably related to uniformly dry surface soil moisture conditions across the landscape and lower topographic variation in midday solar irradiance at higher sun angles.

Spatial variation in daily maximum temperatures was even more pronounced across the montane conifer forest landscape, where inter-site standard deviation in daily *Tmax* often exceeded 20% of the mean. On clear days, sites and microsites could differ by 20 °C or more in daily maximum temperatures. This high level of spatial variation at TEF was also documented by Ma et al. (2010), who observed inter-site differences in soil surface temperatures of up to 30 °C and standard deviations of >3 °C in mean monthly soil surface temperatures from May through August. Ashcroft and Gollan (2013b) reported similar large variation in maximum surface temperatures at a semi-arid western Australian landscape, with site-scale and microsite-scale variation accounting for roughly 60% and 40% of total spatial variance, respectively.

Low microsite spatial variation in daily minimum surface temperatures has been previously reported at TEF (Dingman et al., 2013; Ma et al., 2010), and for other forests and woodlands (e.g., Ashcroft and Gollan, 2013b; Breshears et al., 1998; Frey et al., 2016; Suggitt et al., 2011). We also observed low within-site variation in *Tmin*, but at the site scale we recorded systematically higher or lower minimum temperatures, even over distances of less than 100 m, associated with topography and vegetation cover.

4.2. Dynamic influence of tree canopy density and solar radiation

Incoming shortwave solar radiation is a key driver of diurnal surface energy balance and a primary determinant of spatiotemporal variation in surface temperatures in rugged terrain (Dozier and Outcalt, 1979; Geiger et al., 2009). In the absence of overstory trees, spatial variation in incoming shortwave radiation increases with average slope of the terrain and atmospheric transmittance, and varies dynamically during the course of the day and the year as a function of solar zenith angle (Dubayah et al., 1990). Site-scale (~30-90 m horizontal resolution) models of solar radiation have proven effective for modeling air temperatures at 1 to 2 m above the ground surface, (e.g., Flint et al., 2013; Fridley, 2009; Lookingbill and Urban, 2003; Vanwalleghem and Meentemeyer, 2009). However, we found that modeled surface radiation that did not account for the forest canopy was less effective at predicting site- and microsite-scale surface temperatures than an index of direct understory radiation that accounted for overstory interception of incoming radiation. Much of the site-scale variation in daily maximum temperatures could be predicted with a simple proxy that reduced modeled top-of-canopy solar radiation by fractional canopy density immediately south of the point. The index, which is similar to the direct understory insolation term of Bode et al. (2014), is readily calculated so long as atmospheric transmittance data are available.

Baldocchi et al. (2004) provide a detailed analysis of the dynamic effect of deciduous blue oak canopies on savanna microclimates. Blue oaks at our foothill oak savanna landscape would be expected to have highest Leaf Area Index (LAI) between April and November (Ryu et al., 2012) and maximum gross carbon uptake and evapotranspiration in April through June (Goulden et al., 2012). Ideally we would have multi-date LiDAR imagery to capture the seasonal phenology of these woodlands. Low LAI from November through March may partially explain why modeled canopy density (*CD30*) was associated with lower minimum nighttime temperatures between October and April and higher minimum temperatures from May through September. The negative association of *Tmin* and *CD30* in winter months may be more related to the association of higher tree density with cooler, north-facing slopes and ravines. Microsite-scale influence of canopy density within 5-10 m on daily temperature extremes suggests the highly localized influence of isolated oak canopies on surface microclimates (e.g., Parker and Muller 1982).

The combination of rugged topography and tall, evergreen conifer canopies at the montane forest landscape resulted in pervasive site- and microsite-scale buffering of surface temperature extremes throughout the snow-free period of 2013. The contrast in incident solar radiation at the soil surface between understories and sunlit gaps was presumably much greater in this conifer forest than in foothill oak savanna. One-sided LAI is >7 for *Abies concolor* and *A. magnifica* trees (Westman, 1987). At ecosystem scales, effective tree canopy LAI – which includes all light intercepting canopy elements – ranges from 0 to 1 on the continuum from grassland to *Q. douglasii* woodland (Ryu et al., 2010) compared to 0 to 3.5 on the continuum from gaps to denser tree patches in Sierra mixed-conifer forest (Musselman et al., 2013).

The generally lower model performance for maximum temperatures on clear summer days at the montane forest site could be due to less reliable temperature readings for sensors in hot sunlit areas or the challenge of modeling microsite-scale variation in incoming radiation (sunflecks) on clear days at high elevations (e.g., Ustin et al. 1984). Better prediction of surface temperatures should be obtainable with more complete models of canopy sunlight interception by discontinuous tree canopies (e.g., Bode et al., 2014; Gryning et al., 2001; Musselman et al., 2013). For example, Musselman et al. (2013) present a sophisticated solar raytrace model that calculates light paths through LiDAR-derived 3-dimensional forest structure over heterogeneous terrain. They demonstrate the model using 1-m^3 discrete cubic volumes (voxels) for mixed-conifer forest very similar in structure and composition to Teakettle Experimental Forest, revealing large microsite-scale differences in solar radiation at the surface, even in the tallest (>60 m) conifer forest. A systematic comparison of the power of these different approaches for modeling surface temperature regimes in discontinuous plant canopies would be useful, especially for characterizing the very high microsite-scale variation in surface temperatures associated with Mediterranean-climate ecosystems. We were unsuccessful at predicting this microsite variation in maximum temperatures, although the high correlation between microsite spatial heterogeneity in *UR10* and *Tmax* suggests that it is at least possible to model the magnitude of microsite variation in *Tmax* within sites across these landscapes.

4.3. Dynamic influence of topographic position related to cold-air drainage

In mountainous regions, nocturnal surface cooling is controlled by both fine-scale surface longwave energy balance and larger-scale downslope advection of cold air due to more rapid radiative cooling in highlands vs. lower elevations (Bergen, 1969; Burns and Chemel, 2014; Pypker et al., 2007). Cold-air pooling is well documented in wide valleys of the Sierra Nevada, especially in dry, stable, clear-sky conditions (Lundquist and Cayan, 2007). Our temperature data show evidence of cold-air drainage and perhaps localized shallow pooling – especially in the foothill oak savanna landscape. The montane study landscape lacks large topographic depressions where extensive, deep pooling would be expected (Rambo and North, 2008; Curtis et al., 2014; Lundquist et al., 2008). Accordingly, we suspect the small cold-air effects detected in our analysis are mainly the result of cold-air drainage and, at the montane conifer forest landscape, riparian influence (Rambo and North, 2008; Rambo and North, 2009). Rambo and North (2009) measured air temperatures from 5-45 m above the forest floor at TEF and found that both summer and winter nighttime minimum temperatures were consistently cooler than those in surrounding upland forests. On the other hand, they observed that in summer daytime maximum temperatures in riparian areas tended to be higher than adjacent upland areas, which they attributed to the influence of warm upslope winds. In a related study at TEF, Rambo and North (2008) found that the zone of riparian influence was confined to a few meters horizontally and vertically from the stream channel and noted that effects of local shrubs and trees could dominate over riparian influence. Although our study was not designed to systematically investigate riparian environments, our results generally associate lower position in the landscape with lower daily minimum and maximum surface temperatures. The patterns can vary both seasonally and on a daily basis, and at the montane study landscape (TEF) late summer maximum daytime temperatures were frequently higher in valley and riparian locations. Our models help reveal how much these patterns can vary from day to day, perhaps in relation to variable local wind effects.

The relative elevation metrics proposed by Lundquist et al. (2008) and Ashcroft and Gollan (2013b) were significantly correlated at scales from 150-1000 m (0.34 – 0.86) (Tables A.2, A.3) and both proved effective for modeling spatial variation in surface temperature extremes, although *TPI[500-1000]* yielded better models at the montane forest landscape vs. *TPI250* and *CAP150* at the foothill savanna landscape. The shorter scales at SJER suggest more localized cold-air effects consistent with shorter ridge-to-ridge distances here compared to TEF.

In principle, given average lapse rates in the southern Sierra Nevada of -6-7 °C/km (Lundquist and Cayan, 2007), we would expect elevational cooling effects of 1.2-1.4 °C and 1.0-1.1 °C across our foothill and montane sites, respectively. However, as pointed out by Lundquist and Cayan (2007), lapse rates in the Sierra Nevada can vary dramatically from one day to the next and are highly location-dependent. Within our study landscapes, topographic position or cold-air pooling indices yielded better model predictions for both *Tmax* and *Tmin* than simple elevation, and the direction of the elevation effect was usually inverse to the regional lapse rate. Across both landscapes, sites at lowest relative elevations generally recorded *Tmax* and *Tmin* values that were 1-2 °C cooler than nearby upland sites. Correlations between elevation and *TPI* or *CAP* were low at the montane landscape ($0.03 < |r| < 0.41$) and moderate-to-low at SJER ($0.39 < r < 0.57$), and with more samples across a greater range of elevations we may have been able to tease apart the contrasting influences of average regional lapse rates from local cold-air drainage and riparian effects.

4.4. Modeling variation in site and microsite temperature extremes with NEON AOP LiDAR data

With a small set of LiDAR-derived topographic and canopy variables, we were able to account for, on average, 61-83% of variation in site-scale daily surface temperature extremes. These results compare favorably with other efforts to model surface or near-surface air temperature extremes using ground observations of canopy cover (Ashcroft and Gollan, 2013b) or other small-footprint LiDAR systems (Frey et al., 2016). Our study suggests that NEON AOP data, combined with inexpensive temperature micro-sensor arrays, can be used to monitor and model temperature variation over large areas. This information could increase understanding of microclimates near the ground in heterogeneous landscapes, support calibration and validation of more mechanistic niche models (Kearney and Porter, 2009), and inform spatially explicit population models for improved projections of species vulnerability to climate change (Dullinger et al., 2012; Franklin et al., 2014).

4.5. Cross-scale modeling of thermal microrefugia in mountainous terrain

The complex thermal microclimates in landscapes of the Sierra Nevada are under a hierarchy of controls related to regional weather conditions, environmental lapse rates, topographic position and microsite location relative to vegetation overstory and surface characteristics (Broxton et al., 2015; Dobrowski et al., 2009; Lundquist and Cayan, 2007; Musselman et al., 2013). At very fine microclimate scales, surface temperature regimes can depart significantly from landscape and regional trends and thus provide potential opportunities for species' stepping stones, holdouts or microrefugia under rapid climate change (Hannah et al., 2014), not only in the Sierra Nevada but in mountain landscapes in general. Although our study focused on modeling surface temperatures and did not explicitly account for mediating effects of water availability, soil moisture also covaries with topography and overstory vegetation at site- and microsite scales (e.g., Villegas et al., 2010), adding additional buffering capacity in these landscapes.

The empirical statistical models reported here were fitted to specific landscapes over a single year and are correlative. Nevertheless, they demonstrate the magnitude of fine-scale variation in temperature extremes in these Mediterranean-climate landscapes that must be accounted for when considering climate change effects on species ranges at broader spatial scales, and the mediating influences of local biophysical factors (i.e., microtopography, vegetation structure) on regional climate change exposure (Lenoir et al., 2017). Forest canopy effects on surface temperatures were comparable to or exceeded the effects of topographically induced variation in solar radiation, highlighting the potential for biological moderation of surface temperature regimes associated with regional climate and, by extension, regional climate change (Lenoir et al., 2017; von Arx et al., 2013; Woods et al., 2015). The increasing prevalence of global change-type droughts, however, as well as increasing wildfire activity, has increased forest mortality events across the Sierra Nevada and western North America more generally (e.g., Denison et al., 2014), altering the moderating effects of overstory vegetation and reducing heterogeneity in microclimates and associated species' habitats over large areas.

5. References

Ashcroft, M.B., Gollan, J.R., 2013a. Moisture, thermal inertia, and the spatial distributions of near-surface soil and air temperatures: Understanding factors that promote microrefugia. Agric. For. Meteorol. 176, 77–89. https://doi.org/10.1016/j.agrformet.2013.03.008

Ashcroft, M.B., Gollan, J.R., 2013b. The sensitivity of topoclimatic models to fine-scale microclimatic variability and the relevance for ecological studies. Theor. Appl. Climatol. 1–9.

Asner, G.P., Brodrick, P.G., Anderson, C.B., Vaughn, N., Knapp, D.E., Martin, R.E., 2016. Progressive forest canopy water loss during the 2012–2015 California drought. Proc. Natl. Acad. Sci. 113, E249–E255. https://doi.org/10.1073/pnas.1523397113

Baldocchi, D.D., L. Xu, N. Kiang, 2004. How plant functional-type, weather, seasonal drought, and soil physical properties alter water and energy fluxes of an oak–grass savanna and an annual grassland. Agric. For. Meteorol. 123,13-39. https://doi.org/10.1016/j.agrformet.2003.11.006

Barry, R.G., 1970. A framework for climatological research with particular reference to scale concepts. Trans. Inst. Br. Geogr. 49, 61–70. https://doi.org/10.2307/621641

Belsky, A.J., Mwonga, S.M., Amundson, R.G., Duxbury, J.M., Ali, A.R., 1993. Comparative effects of isolated trees on their undercanopy environments in high-rainfall and low-rainfall savannas. J. Appl. Ecol. 30, 143–155. https://doi.org/10.2307/2404278

Bergen, J.D., 1969. Cold air drainage on a forested mountain slope. J. Appl. Meteorol. 8, 884–895. https://doi.org/10.1175/1520-0450(1969)008<0884:CADOAF>2.0.CO;2

Bode, C.A., Limm, M.P., Power, M.E., Finlay, J.C., 2014. Subcanopy Solar Radiation model: Predicting solar radiation across a heavily vegetated landscape using LiDAR and GIS solar radiation models. Remote Sens. Environ. 154, 387–397. https://doi.org/10.1016/j.rse.2014.01.028

Breshears, D.D., 2006. The grassland-forest continuum: Trends in ecosystem properties for woody plant mosaics? Front. Ecol. Environ. 4, 96–104. http://www.jstor.org/stable/3868713

Breshears, D.D., Nyhan, J.W., Heil, C.E., Wilcox, B.P., 1998. Effects of woody plants on microclimate in a semiarid woodland: Soil temperature and evaporation in canopy and intercanopy patches. Int. J. Plant Sci. 159, 1010–1017. https://doi.org/10.1086/314083

Broxton, P.D., Harpold, A.A., Biederman, J.A., Troch, P.A., Molotch, N.P., Brooks, P.D., 2015. Quantifying the effects of vegetation structure on snow accumulation and ablation in mixed-conifer forests. Ecohydrology 8, 1073–1094. https://doi.org/10.1002/eco.1565

Burns, P., Chemel, C., 2014. Evolution of cold-air-pooling processes in complex terrain. Bound.-Layer Meteorol. 150, 423–447. https://doi.org/10.1007/s10546-013-9885-z

Chen, J., Saunders, S.C., Crow, T.R., Naiman, R.J., Brosofske, K.D., Mroz, G.D., Brookshire, B.L., Franklin, J.F., 1999. Microclimate in forest ecosystem and landscape ecology. BioScience 49, 288–297. https://doi.org/10.2307/1313612

Curtis, J.A., Flint, L.E., Flint, A.L., Lundquist, J.D., Hudgens, B., Boydston, E.E., Young, J.K., 2014. Incorporating cold-air pooling into downscaled climate models increases potential refugia for snow-dependent species within the Sierra Nevada Ecoregion, CA. PLoS ONE 9, e106984. https://doi.org/10.1371/journal.pone.0106984

Davis, F.W., Sweet, L.C., Serra-Diaz, J.M., Franklin, J., McCullough, I., Flint, A., Flint, L., Dingman, J.R., Regan, H.M., Syphard, A.D., Hannah, L., Redmond, K., Moritz, M.A., 2016. Shrinking windows of opportunity for oak seedling establishment in southern California mountains. Ecosphere 7, 1–18. https://doi.org/10.1002/ecs2.1573

Dennison, P.E., Brewer, S.C., Arnold, J.D., Moritz, MA., 2014. Large wildfire trends in the western United States, 1984–2011. Geophys. Res. Lett. 41, 2928-2933. https://doi.org/10.1002/2014GL059576

Dingman, J.R., Sweet, L.C., McCullough, I., Davis, F.W., Flint, A., Franklin, J., Flint, L.E., 2013. Cross-scale modeling of surface temperature and tree seedling establishment in mountain landscapes. Ecol. Process. 2, 1–15. https://doi.org/10.1186/2192-1709-2-30

Dobrowski, S.Z., 2011. A climatic basis for microrefugia: The influence of terrain on climate. Glob. Change Biol. 17, 1022–1035. https://doi.org/10.1111/j.1365-2486.2010.02263.x

Dobrowski, S.Z., Abatzoglou, J.T., Greenberg, J.A., Schladow, S.G., 2009. How much influence does landscape-scale physiography have on air temperature in a mountain environment? Agric. For. Meteorol. 149, 1751–1758. https://doi.org/10.1016/j.agrformet.2009.06.006

Dozier, J., Outcalt, S.I., 1979. An approach toward energy balance simulation over rugged terrain. Geogr. Anal. 11, 65–85. https://doi.org/10.1111/j.1538-4632.1979.tb00673.x

Dubayah, R., Dozier, J., Davis, F.W., 1990. Topographic distribution of clear-sky radiation over the Konza Prairie, Kansas. Water Resour. Res. 26, 679–690. https://doi.org/10.1029/WR026i004p00679

Dullinger, S., Gattringer, A., Thuiller, W., Moser, D., Zimmermann, N.E., Guisan, A., Willner, W., Plutzar, C., Leitner, M., Mang, T., Caccianiga, M., Dirnböck, T., Ertl, S., Fischer, A., Lenoir, J., Svenning, J.-C., Psomas, A., Schmatz, D.R., Silc, U., Vittoz, P., Hülber, K., 2012. Extinction debt of high-mountain plants under twenty-first-century climate change. Nat. Clim. Change 2, 619–622. https://doi.org/10.1038/nclimate1514

Eitel, J.U.H., Höfle, B., Vierling, L.A., Abellán, A., Asner, G.P., Deems, J.S., Glennie, C.L., Joerg, P.C., LeWinter, A.L., Magney, T.S., Mandlburger, G., Morton, D.C., Müller, J., Vierling, K.T., 2016. Beyond 3-D: The new spectrum of lidar applications for earth and ecological sciences. Remote Sens. Environ. 186, 372–392. https://doi.org/10.1016/j.rse.2016.08.018

Elith, J., Leathwick, J.R., Hastie, T., 2008. A working guide to boosted regression trees. J. Anim. Ecol. 77, 802–813. https://doi.org/10.1111/j.1365-2656.2008.01390.x

Flint, A.L., Childs, S.W., 1987. Calculation of solar radiation in mountainous terrain. Agric. For. Meteorol. 40, 233–249. https://doi.org/10.1016/0168-1923(87)90061-X

Flint, L.E., Flint, A.L., Thorne, J.H., Boynton, R., 2013. Fine-scale hydrologic modeling for regional landscape applications: the California Basin Characterization Model development and performance. Ecol. Process. 2, 25. https://doi.org/10.1186/2192-1709-2-25

Ford, K.R., Ettinger, A.K., Lundquist, J.D., Raleigh, M.S., Hille Ris Lambers, J., 2013. Spatial heterogeneity in ecologically important climate variables at coarse and fine scales in a high-snow mountain landscape. PLoS ONE 8, e65008. https://doi.org/10.1371/journal.pone.0065008

Franklin, J., Regan, H.M., Syphard, A.D., 2014. Linking spatially explicit species distribution and population models to plan for the persistence of plant species under global change. Environ. Conserv. 41, 97–109. https://doi.org/10.1017/S0376892913000453

Frey, S.J.K., Hadley, A.S., Johnson, S.L., Schulze, M., Jones, J.A., Betts, M.G., 2016. Spatial models reveal the microclimatic buffering capacity of old-growth forests. Sci. Adv. 2, e1501392–e1501392. https://doi.org/10.1126/sciadv.1501392

Fridley, J.D., 2009. Downscaling climate over complex terrain: High finescale (< 1000 m) spatial variation of near-ground temperatures in a montane forested landscape (Great Smoky Mountains). J. Appl. Meteorol. Climatol. 48, 1033–1049. https://doi.org/10.1175/2008JAMC2084.1

Fu, P., Rich, P., 2002. A geometric solar radiation model with applications in agriculture and forestry. Comput. Electron. Agric. 37, 25–35. https://doi.org/10.1016/S0168-1699(02)00115-1

Geiger, R., Aron, R.H., Todhunter, P., 2009. The climate near the ground, 7th ed. Rowman & Littlefield Pub. Group, Lanham, Md.

Goulden, M.L., Anderson, R.G., Bales, R.C., Kelly, A.E., Meadows, M., Winston, G.C., 2012. Evapotranspiration along an elevation gradient in California's Sierra Nevada. J. Geophys. Res.-Biogeosciences 117, 13. https://doi.org/10.1029/2012jg002027

Goulden, M.L., Kelley, A., 2016. CZO Dataset: Flux Tower Transect, SJER - Flux Tower, Meteorology (2009-2016) [WWW Document]. URL http://criticalzone.org/sierra/data/dataset/3657/ (accessed 12.27.16).

Goulden, M.L., Kelley, A., 2015. CZO Dataset: Flux Tower Transect, P301 - Flux Tower, Meteorology (2007-2015) [WWW Document]. URL http://criticalzone.org/sierra/data/dataset/3654/ (accessed 12.27.16).

Graae, B.J., De Frenne, P., Kolb, A., Brunet, J., Chabrerie, O., Verheyen, K., Pepin, N., Heinken, T., Zobel, M., Shevtsova, A., 2012. On the use of weather data in ecological studies along altitudinal and latitudinal gradients. Oikos 121, 3–19. https://doi.org/10.1111/j.16000706.2011.19694.x

Gryning, S.-E., Batchvarova, E., Bruin, H.A.R.D., 2001. Energy Balance Of A Sparse Coniferous High-Latitude Forest Under Winter Conditions. Bound.-Layer Meteorol. 99, 465–488. https://doi.org/10.1023/A:1018939329915

Hannah, L., Flint, L., Syphard, A.D., Moritz, M.A., Buckley, L.B., McCullough, I.M., 2014. Fine-grain modeling of species' response to climate change: Holdouts, stepping-stones, and microrefugia. Trends Ecol. Evol. 29, 390–397. https://doi.org/10.1016/j.tree.2014.04.006

Hastie, T., Tibshirani, R., Friedman, J.H., 2009. The elements of statistical learning: data mining, inference, and prediction, 2nd ed. ed, Springer series in statistics. Springer, New York, NY.

Holden, Z.A., Klene, A.E., F. Keefe, R., G. Moisen, G., 2013. Design and evaluation of an inexpensive radiation shield for monitoring surface air temperatures. Agric. For. Meteorol. 180, 281–286. https://doi.org/10.1016/j.agrformet.2013.06.011

Kampe, T.U., Johnson, B.R., Kuester, M.A., Keller, M., 2010. NEON: the first continental-scale ecological observatory with airborne remote sensing of vegetation canopy biochemistry and structure. J. Appl. Remote Sens. 4, 043510. https://doi.org/10.1117/1.3361375

Kampe, T.U., Leisso, N., Musinsky, J., Petroy, S., Karpowicza, B., Krause, K., Crocker, R.I., DeVoe, M., Penniman, E., Guadagno, T., Gallery, W., Ramond, T., Wasser, L., Barnett, D., van Aardt, J., Cawse-Nicholson, K., Serbin, S.P., 2013. The NEON 2013 Airborne Campaign at

Domain 17 Terrestrial and Aquatic Sites in California (NEON Technical Memo No. 005), http://www.neoninc.org/sites/default/files/bibliofiles/TM-005.pdf

Kearney, M., Porter, W., 2009. Mechanistic niche modelling: combining physiological and spatial data to predict species' ranges. Ecol. Lett. 12, 334–350. https://doi.org/10.1111/j.14610248.2008.01277.x

Kuhn, M., 2017. A short introduction to the caret package [WWW Document]. URL http://cran.r-project.org/web/packages/caret/vignettes/caret.pdf (accessed 9.25.17).

Lenoir, J., Hattab, T., Pierre, G., 2017. Climatic microrefugia under anthropogenic climate change: implications for species redistribution. Ecography 40, 253–266. https://doi.org/10.1111/ecog.02788

Lookingbill, T.R., Urban, D.L., 2003. Spatial estimation of air temperature differences for landscape-scale studies in montane environments. Agric. For. Meteorol. 114, 141–151. https://doi.org/10.1016/S0168-1923(02)00196-X

Lundquist, J.D., Cayan, D.R., 2007. Surface temperature patterns in complex terrain: Daily variations and long-term change in the central Sierra Nevada, California. J. Geophys. Res. 112, D11124. https://doi.org/10.1029/2006JD007561

Lundquist, J.D., Pepin, N., Rochford, C., 2008. Automated algorithm for mapping regions of cold-air pooling in complex terrain. J. Geophys. Res. 113. https://doi.org/10.1029/2008JD009879

Ma, S., Oakley, B., North, M., Chen, J., 2010. Spatial variability in microclimate in a mixed-conifer forest before and after thinning and burning treatments. For. Ecol. Manag. 259, 904–915. https://doi.org/10.1016/j.foreco.2009.11.030

Martens, S.N., Breshears, D.D., Meyer, C.W., 2000. Spatial distributions of understory light along the grassland/forest continuum: effects of cover, height, and spatial pattern of tree canopies. Ecol. Model. 126, 79–93. https://doi.org/10.1016/S0304-3800(99)00188-X

Musselman, K.N., Margulis, S.A., Molotch, N.P., 2013. Estimation of solar direct beam transmittance of conifer canopies from airborne LiDAR. Remote Sens. Environ. 136, 402–415. https://doi.org/10.1016/j.rse.2013.05.021

North, M., Oakley, B., Chen, J., Erickson, H., Gray, A., Izzo, A., Johnson, D., Ma, S., Marra, J., Meyers, M., Purcell, K., Rambo, T., Rizzo, D., Roath, B., Schowalter, T., 2010. Vegetation and ecological characteristics of mixed-conifer and Red Fir forests at the Teakettle Experiemental Forest (Technical Report PSW-GTR-186). USDA Forest Service. Pacific Southwest Research Station.

Parker, V.T., Muller, C.H., 1982. Vegetational and environmental changes beneath isolated live oak trees (*Quercus agrifolia*) in a California annual grasslands. Am. Midl. Nat. 107, 69–81. https://doi.org/10.2307/2425189

Pierson, F.B., Wight, J.R., 1991. Variability of near-surface soil temperature on sagebrush rangeland. J. Range Manag. 44, 491–497. https://doi.org/10.2307/4002751

Pypker, T.G., Unsworth, M.H., Mix, A.C., Rugh, W., Ocheltree, T., Alstad, K., Bond, B.J., 2007. Using nocturnal cold air drainage flow to monitor ecosystem processes in complex terrain. Ecol. Appl. 17, 702–714. https://doi.org/10.1890/05-1906

Rambo, T.R., North, M.P., 2008. Spatial and Temporal Variability of Canopy Microclimate in a Sierra Nevada Riparian Forest. Northwest Sci. 82, 259–268. https://doi.org/10.3955/0029-344X-82.4.259

Rambo, T.R., North, M.P., 2009. Canopy microclimate response to pattern and density of thinning in a Sierra Nevada forest. For. Ecol. Manag. 257, 435–442. https://doi.org/10.1016/j.foreco.2008.09.029

Ridgeway, G., 2007. Generalized Boosted Models: A guide to the gbm package [WWW Document]. URL http: //cran.r- project. org/ web/ packages/ gbm/ vignettes/gbm.pdf (accessed 9.25.17).

Robeson, S.M., 2015. Revisiting the recent California drought as an extreme value. Geophys. Res. Lett. 42, 6771–6779. https://doi.org/10.1002/2015GL064593

Rosenberg, N.J., Blad, B.L., Verma, S.B., 1983. Microclimate; The biological environment 2nd ed. Wiley-Interscience, New York.

Ryu, Y., Sonnentag, O., Nilson, T., Vargas, R., Kobayashi, H., Wenk, R., Baldocchi, D.D., 2010. How to quantify tree leaf area index in an open savanna ecosystem: A multi-instrument and multi-model approach. Agric. For. Meteorol. 150, 63–76. https://doi.org/10.1016/j.agrformet.2009.08.007

Ryu, Y., Verfaillie, J., Macfarlane, C., Kobayashi, H., Sonnentag, O., Vargas, R., Ma, S., Baldocchi, D.D., 2012. Continuous observation of tree leaf area index at ecosystem scale using upward-pointing digital cameras. Remote Sens. Environ. 126, 116–125. https://doi.org/10.1016/j.rse.2012.08.027

Scherrer, D., Körner, C., 2011. Topographically controlled thermal-habitat differentiation buffers alpine plant diversity against climate warming. J. Biogeogr. 38, 406–416. https://doi.org/10.1111/j.1365-2699.2010.02407.x

Schmidt, M., Jochheim, H., Kersebaum, K.-C., Lischeid, G., Nendel, C., 2017. Gradients of microclimate, carbon and nitrogen in transition zones of fragmented landscapes – a review. Agric. For. Meteorol. 232, 659–671. https://doi.org/10.1016/j.agrformet.2016.10.022

Serra-Diaz, J.M., Franklin, J., Sweet, L.C., McCullough, I.M., Syphard, A.D., Regan, H.M., Flint, L.E., Flint, A.L., Dingman, J.R., Moritz, M., Redmond, K., Hannah, L., Davis, F.W., 2016. Averaged 30 year climate change projections mask opportunities for species establishment. Ecography 39, 844–845. https://doi.org/10.1111/ecog.02074

Suggitt, A.J., Gillingham, P.K., Hill, J.K., Huntley, B., Kunin, W.E., Roy, D.B., Thomas, C.D., 2011. Habitat microclimates drive fine-scale variation in extreme temperatures. Oikos 120, 1–8. https://doi.org/10.1111/j.1600-0706.2010.18270.x

Ustin, S.L., R.A. Woodward, M.G. Barbour, J.T. Hatfield, 1984. Relationships between sunfleck dynamics and red fir seedling distribution. Ecology 65: 1420-1428. https://www.jstor.org/stable/1939122

Vanwalleghem, T., Meentemeyer, R., 2009. Predicting forest microclimate in heterogeneous landscapes. Ecosystems 12, 1158–1172. https://doi.org/10.1007/s10021-009-9281-1

von Arx, G., Graf Pannatier, E., Thimonier, A., Rebetez, M., 2013. Microclimate in forests with varying leaf area index and soil moisture: potential implications for seedling establishment in a changing climate. J. Ecol. 101, 1201–1213. https://doi.org/10.1111/1365-2745.12121

Villegas, J.C., D.D. Breshears, C.B. Lou, D.J. Larin., 2010. Ecohydrological controls of soil evaporation in deciduous drylands: How the hierarchical effects of litter, patch and vegetation mosaic cover interact with phenology and season. J. Arid Env. 74: 595-602. https://doi.org/10.1016/j.jaridenv.2009.09.028

Westman, W.E., 1987. Aboveground biomass, surface area, and production relations of red fir (*Abies magnified*) and white fir (*A* . *concolor*). Can. J. For. Res. 17, 311–319. https://doi.org/10.1139/x87-052

Woods, H.A., Dillon, M.E., Pincebourde, S., 2015. The roles of microclimatic diversity and of behavior in mediating the responses of ectotherms to climate change. J. Therm. Biol. 54, 86–97. https://doi.org/10.1016/j.jtherbio.2014.10.002

6. Acknowledgements

Funding was provided by the U.S. National Science Foundation (EF-1065864, -1550653, -1065826 and -1550640). Sabbatical office space and computing support for F. Davis during manuscript preparation were provided by the Department of Earth and Environment at Boston University. We thank participants in NSF Project EF-1065864, Macrosystems Biology Program grant "Do microenvironments govern macroecology") for discussions that led to many of the ideas and analyses undertaken in this research and for help with field equipment installation and data collection, notably: Lorrie Flint, Lee Hannah, Elizabeth Hiroyasu, Eric Hopkins, Andy MacDonald, Sean McKnight, Jason McClure, Malcolm North, Phoebe Prather, Kelly Redmond (deceased), Anderson Shepard, Peter Slaughter, Lynn Sweet, and Whitney Wilkinson. Flux tower data were provided by the NSF-supported Southern Sierra Critical Zone Observatory. We thank Tristan Goulden and Nathan Leisso at NEON, Inc., for providing data, advice and support. Thanks also to two anonymous reviewers for their helpful comments on the draft manuscript.

Table 1. Summary of daily surface temperature extremes at the foothill oak savanna landscape (SJER) and montane forest landscape (TEF) for 2013. Entries are the means of daily values for the indicated monthly time periods.

	Foothill (SJER)				Montane (TEF)			
Month	T_{min} (°C)	CV (%)	T_{max} (°C)	CV (%)	T_{min} (°C)	CV(%)	T_{max} (°C)	CV (%)
Jan - Mar	3.3	33	24.8	13	NA	NA	NA	NA
Apr	8.7	32	38.6	12	0.2	57	23.5	25
May	12.0	15	45.2	8	2.8	148	28.2	15
Jun	16.7	10	51.1	6	7.8	24	35.6	10
Jul	21.0	8	54.8	5	11.6	11	39.3	9
Aug	17.7	10	52.2	6	9.1	17	38.4	10
Sep	15.1	12	47.0	8	6.8	12	32.9	15
Oct-Dec	5.5	17	31.2	14	NA	NA	NA	NA

Fig. 1. Location map for San Joaquin Experimental Range (SJER) and Teakettle Experimental Forest (TEF) study landscapes. Elevations from the San Joaquin Valley floor up the western slope of the Sierra Nevada are displayed on shaded relief.

Fig 2. Photos of Teakettle Experimental Forest a) north-slope and b) south-slope sites, and San Joaquin Experimental Range c) north-slope and d) south-slope sites illustrating the difference in vegetation structure at the two landscapes. Fenced experimental gardens and a subset of the surface temperature sensors (vertical posts) in site sensor arrays are also visible.

Fig. 3. Surface temperature sensor locations at a) foothill savanna landscape, San Joaquin Experimental Range (SJER) and (b) montane forest landscape, Teakettle Experimental Forest (TEF). Yellow triangles are locations of single temperature sensors and open white circles are locations of 21-sensor arrays. Background is shaded relief, illuminated from due south. LiDAR-derived tree crowns are displayed as two height classes, < 25m (light green) and >25m (dark green).

Fig. 4. Spatial arrangement of temperature sensors (closed dot) and weather station (open dot) in and around experimental gardens (open square) used to characterize microsite temperature variation.

Fig. 5. Time series of daily maximum (red) and minimum (blue) surface temperatures at (a) foothill oak savanna, San Joaquin Experimental Range (SJER), and (b) montane conifer forest, Teakettle Experimental Forest (TEF), for the 2013 calendar year. Daily temperatures at 24 sites at TEF and 18 sites at SJER are displayed; vertical line length shows the daily temperature range among sites. Dashed vertical lines divide months shown on the X-axis.

Fig. 6. Loess-smoothed average maximum daily surface temperatures and standard deviations (shaded bands) for sensor arrays at 6 sites at (a) the San Joaquin Experimental Range foothill oak savanna landscape and (b) Teakettle Experimental Forest montane conifer forest landscape. Labels indicate the topographic positions of the arrays (N – north facing, NE – northeast, L – level, VF, valley floor, S – south, SW – southwest).

Fig. 7. Generalized boosted model results relating daily site-scale maximum temperatures (*Tmax*) in the foothill savanna landscape (SJER) to (a) modeled understory radiation (*UR30*) and (b) a cold-air

drainage index (*TPI250*); Partial model dependence on *UR30* and *TPI250* is the difference in predicted temperatures at lowest and highest observed values of the predictor variable. (c) Model adjusted r^2, the squared correlation between predicted and observed temperatures for each daily model.

Fig. 8. Generalized boosted model results for daily site-scale minimum temperatures (*Tmin*) at San Joaquin Experimental Range (SJER) showing model partial dependence on (a) canopy density (*CD30*) and (b) a cold-air drainage index (*CAP150*) as well as (c) model adjusted r^2 for each daily model.

Fig. 9. Generalized boosted model results for daily microsite-scale minimum temperatures (*Tmin*) at San Joaquin Experimental Range (SJER) showing model partial dependence on (a) microsite canopy density (*CD10*) and slope angle (*S*), as well as (c) model adjusted r^2 for each daily model.

Fig. 10. Generalized boosted model (GBM) results for (a) daily site-scale maximum surface temperatures (*Tmax*) at Teakettle Experimental Forest (TEF) showing model partial dependence on (top panel) modeled understory radiation (*UR30*) and (middle panel) a cold-air drainage index (*TPI500*), as well as (bottom panel) model adjusted r^2 for 183 daily models between April 1 and September 30, 2013. (b) GBM results for daily site-scale minimum surface temperatures (*Tmin*) at TEF in relation to (top panel) tree canopy density (*CD30*) and (middle panel) *TPI500*; (bottom panel) daily model adjusted r^2.

Supplementary Materials

Table A.1. Screening criteria used to delete daily temperature data records that were deemed potentially unreliable.

1. Logger temperature changed by more than 20 °C in any 60 minute period – daily record removed.
2. Recorded temperature remained identical for ten or more readings – daily record removed.
3. For sensors in garden arrays, single temperature reading was more than 5 °C above or below daily maximum or minimum values for any other sensor in the garden array. This process was run repeatedly until no more daily records could be removed.
4. If sensor daily temperatures remained in the range -2 °C to 2 °C, it was assumed that the sensor was submerged in snow and that sensor's daily record was removed.
5. If physical sensor issues or data download issues were noted during manual data download, data were manually inspected and suspicious daily records were removed.

Table A.2. Correlation matrix, LIDAR-derived measures for Teakettle Experimental Forest (TEF) temperature monitoring sites (n=24), including elevation (DEM), tree canopy density (CD) at 30, 60 and 90m scales, cold-air pooling index (CAP) at 150, 250, 500 and 1000m scales, and topographic position index (TPI) at 150, 250,500 and 1000m scales. Entries in bold are significant at p <0.05.

	DEM	**CD30**	**CD60**	**CD90**	**CAP150**	**CAP250**	**CAP500**	**CAP1000**	**TPI150**	**TPI250**	**TPI500**	**TPI1000**
DEM	1	0.37	**0.47**	**0.53**	0.33	0.18	-0.06	-0.26	0.05	0.14	0.41	0.24
CD30	0.37	1	**0.91**	**0.86**	-0.09	-0.08	-0.23	-0.36	-0.17	-0.24	-0.34	-0.2
CD60	**0.47**	**0.91**	1	**0.96**	-0.12	-0.07	-0.28	-0.39	-0.21	-0.29	-0.31	-0.19
CD90	**0.53**	**0.86**	**0.96**	1	-0.11	-0.14	-0.33	**-0.46**	-0.26	-0.32	-0.22	-0.24
CAP150	0.33	-0.09	-0.12	-0.11	1	0.7	**0.63**	**0.45**	**0.46**	**0.52**	**0.58**	**0.57**
CAP250	0.18	-0.08	-0.07	-0.14	**0.7**	1	**0.9**	**0.67**	**0.68**	**0.7**	0.34	**0.76**
CAP500	-0.06	-0.23	-0.28	-0.33	**0.63**	**0.9**	1	**0.79**	**0.73**	**0.75**	**0.42**	**0.78**
CAP1000	-0.26	-0.36	-0.39	**-0.46**	**0.45**	**0.67**	**0.79**	1	**0.56**	**0.59**	**0.42**	**0.86**
TPI150	0.05	-0.17	-0.21	-0.26	**0.46**	**0.68**	**0.73**	**0.56**	1	**0.96**	**0.51**	**0.67**
TPI250	0.14	-0.24	-0.29	-0.32	**0.52**	**0.7**	**0.75**	**0.59**	**0.96**	1	**0.66**	**0.75**
TPI500	0.41	-0.34	-0.31	-0.22	**0.58**	0.34	**0.42**	**0.42**	**0.51**	**0.66**	1	**0.66**
TPI1000	0.24	-0.2	-0.19	-0.24	**0.57**	**0.76**	**0.78**	**0.86**	**0.67**	**0.75**	**0.66**	1

Table A.3. Correlation matrix, LIDAR-derived measures for San Joaquin Experimental Range (SJER) temperature monitoring sites (n=18), including elevation (ELEV), tree canopy density (CD) at 30, 60 and 90m scales, cold-air pooling index (CAP) at 150, 250, 500 and 1000m scales, and topographic position index (TPI) at 150, 250,500 and 1000m scales. Entries in bold are significant at $p <0.05$.

	DEM	**CD30**	**CD60**	**CD90**	**CAP150**	**CAP250**	**CAP500**	**CAP1000**	**TPI150**	**TPI250**	**TPI500**	**TPI1000**
DEM	1	0.3	0.42	0.44	**0.53**	**0.52**	**0.49**	0.46	0.43	0.5	**0.57**	0.39
CD30	0.3	1	**0.92**	**0.86**	0.14	0.06	-0.05	-0.05	-0.1	-0.13	-0.16	0.02
CD60	0.42	**0.92**	1	**0.98**	0.15	0.07	-0.06	-0.09	-0.07	-0.1	-0.1	0.05
CD90	0.44	**0.86**	**0.98**	1	0.11	0.04	-0.1	-0.14	-0.12	-0.14	-0.12	-0.01
CAP150	**0.53**	0.14	0.15	0.11	1	**0.97**	**0.87**	**0.78**	**0.64**	**0.75**	**0.83**	**0.61**
CAP250	**0.52**	0.06	0.07	0.04	**0.97**	1	**0.86**	**0.78**	**0.7**	**0.81**	**0.86**	**0.65**
CAP500	**0.49**	-0.05	-0.06	-0.1	**0.87**	**0.86**	1	**0.95**	**0.67**	**0.78**	**0.87**	**0.6**
CAP1000	0.46	-0.05	-0.09	-0.14	**0.78**	**0.78**	**0.95**	1	**0.67**	**0.77**	**0.85**	**0.58**
TPI150	0.43	-0.1	-0.07	-0.12	**0.64**	**0.7**	**0.67**	**0.67**	1	**0.96**	**0.8**	**0.96**
TPI250	**0.5**	-0.13	-0.1	-0.14	**0.75**	**0.81**	**0.78**	**0.77**	**0.96**	1	**0.92**	**0.88**
TPI500	**0.57**	-0.16	-0.1	-0.12	**0.83**	**0.86**	**0.87**	**0.85**	**0.8**	**0.92**	1	**0.67**
TPI1000	0.39	0.02	0.05	-0.01	**0.61**	**0.65**	**0.6**	**0.58**	**0.96**	**0.88**	**0.67**	1

Captions for Supplementary Figures

Fig. A.1. Spatial variation in *Tmax*, measured as the standard deviation of maximum daily temperature, across (a) 18 sites at the foothill savanna site, San Joaquin Experimental Range (SJER), and (b) the montane forest site, Teakettle Experimental Forest, as a function of day of the year, January 1 – December 31, 2013. Loess locally-weighted regression line ± standard error (shaded region) are also shown. Note the change in horizontal scale, as indicated by arrows. Temperature data were only analyzed from day 91 to 273 at TEF.

Fig. A.2. Loess-smoothed minimum daily surface temperatures (*Tmin*) and standard deviations (shaded areas) for sensor arrays at 6 sites at the foothill oak savanna landscape (SJER, top panel) and montane conifer forest landscape (TEF, lower panel). Labels indicate the topographic positions of the arrays (N – north facing, NE – northeast, L – low slope, VF, valley floor, S – south, SW – southwest).

Fig. A.3. Predicted versus observed within-array standard deviation in daily *Tmax* at the foothill savanna landscape, San Joaquin Experimental Range. Results are for a linear mixed model with garden array as a random effect and an index of microsite understory radiation (UR5) as a fixed effect. Daily values for different gardens are plotted as different colors for arrays located on south slope (S), valley floor (VF), level (L), southwest slope (SW), northeast slope (NE) and north (N).

Fig. A.4. Relationship between model fit (adjusted r^2) and atmospheric transmittance for generalized boosted models of site-scale *Tmax* at TEF. The line is a locally weighted regression line with standard error ribbon.

Fig. A.5. Predicted versus observed within-array standard deviation (SD) in daily *Tmax* at the montane conifer forest landscape, Teakettle Experimental Forest (TEF). Results are for a linear mixed model with garden array as a random effect and an index of microsite understory radiation (UR10) and fractional ground cover within 5 m south of the sensor (GCs5) as fixed variables. Daily values for different gardens are plotted as different colors for arrays located on south slope (S), valley floor (VF), level (L), southwest slope (SW), northeast slope (NE) and north slope (N).

Figure 1.

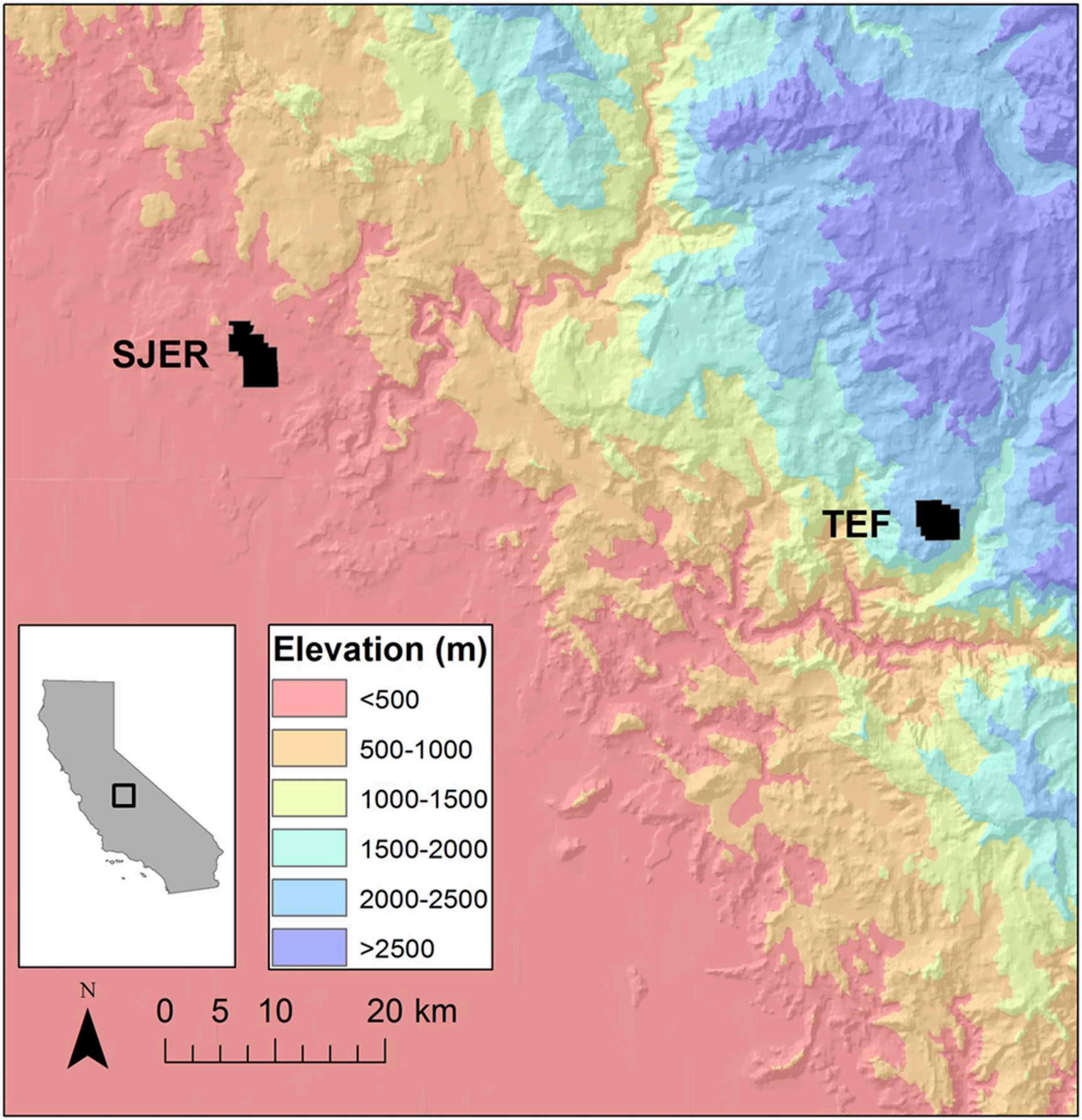
SJER
TEF
Elevation (m)
<500
500-1000
1000-1500
1500-2000
2000-2500
>2500
N
0 5 10 20 km

Figure 2

Figure 3

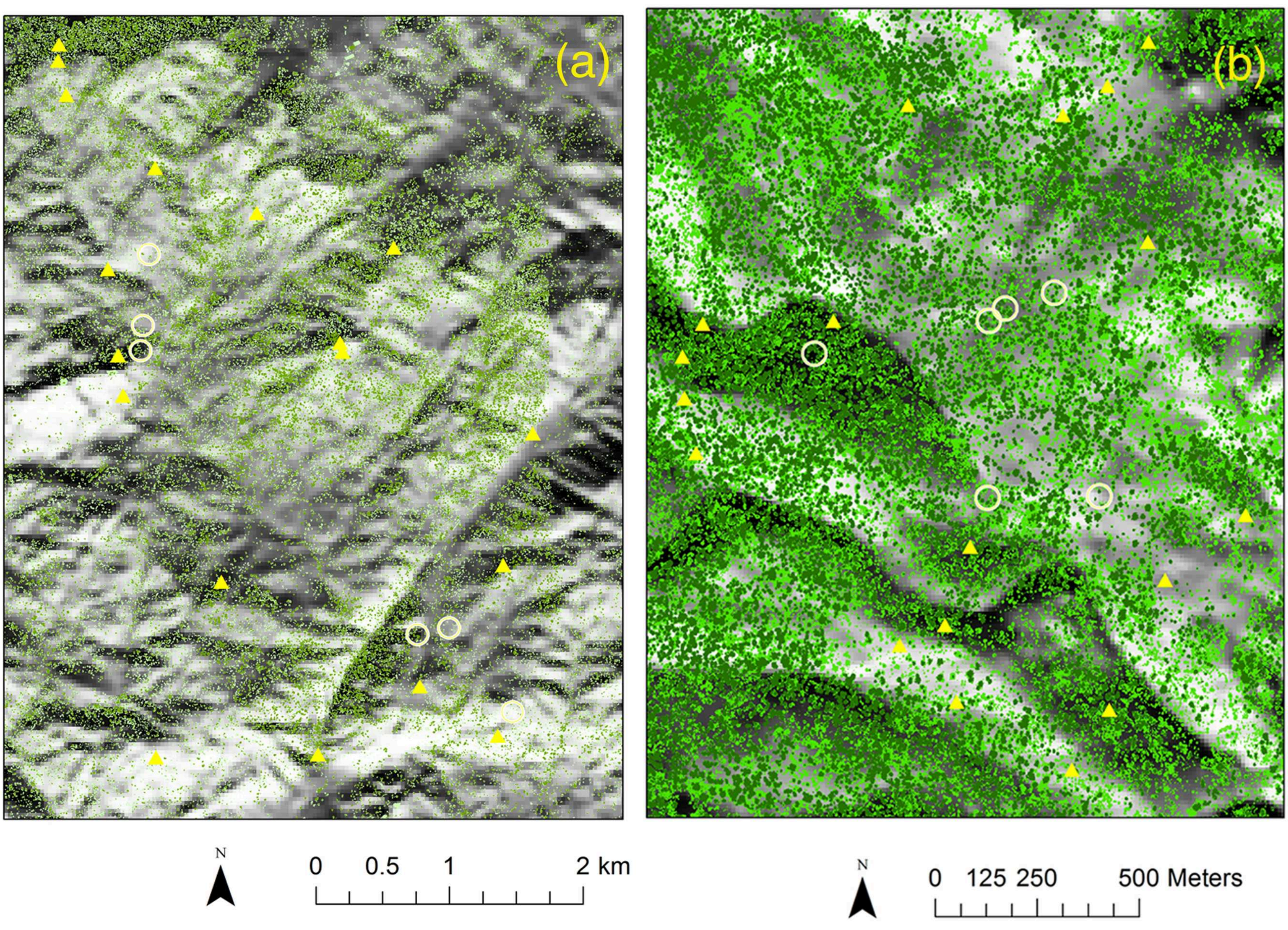

Figure 4

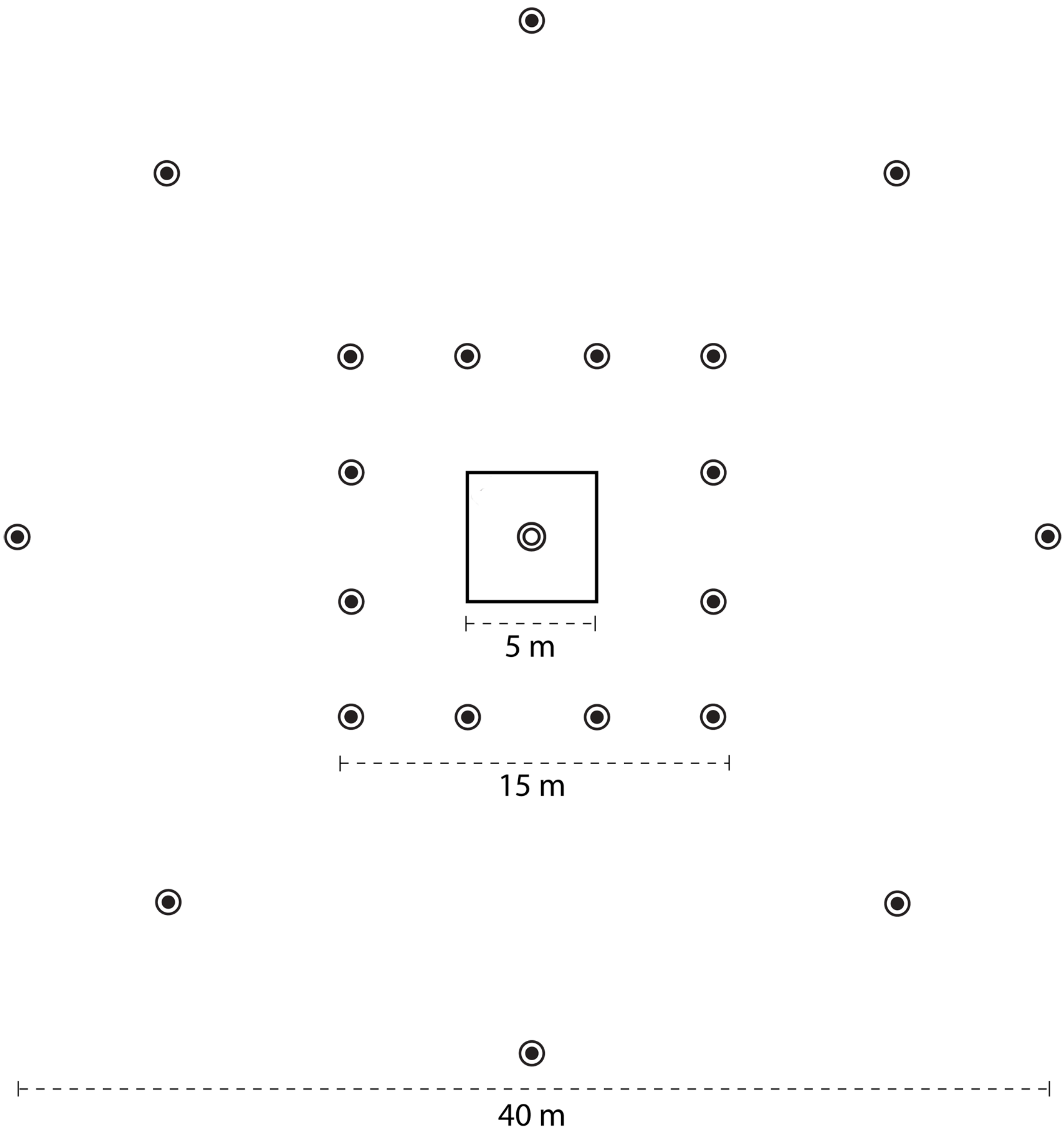

Figure 5

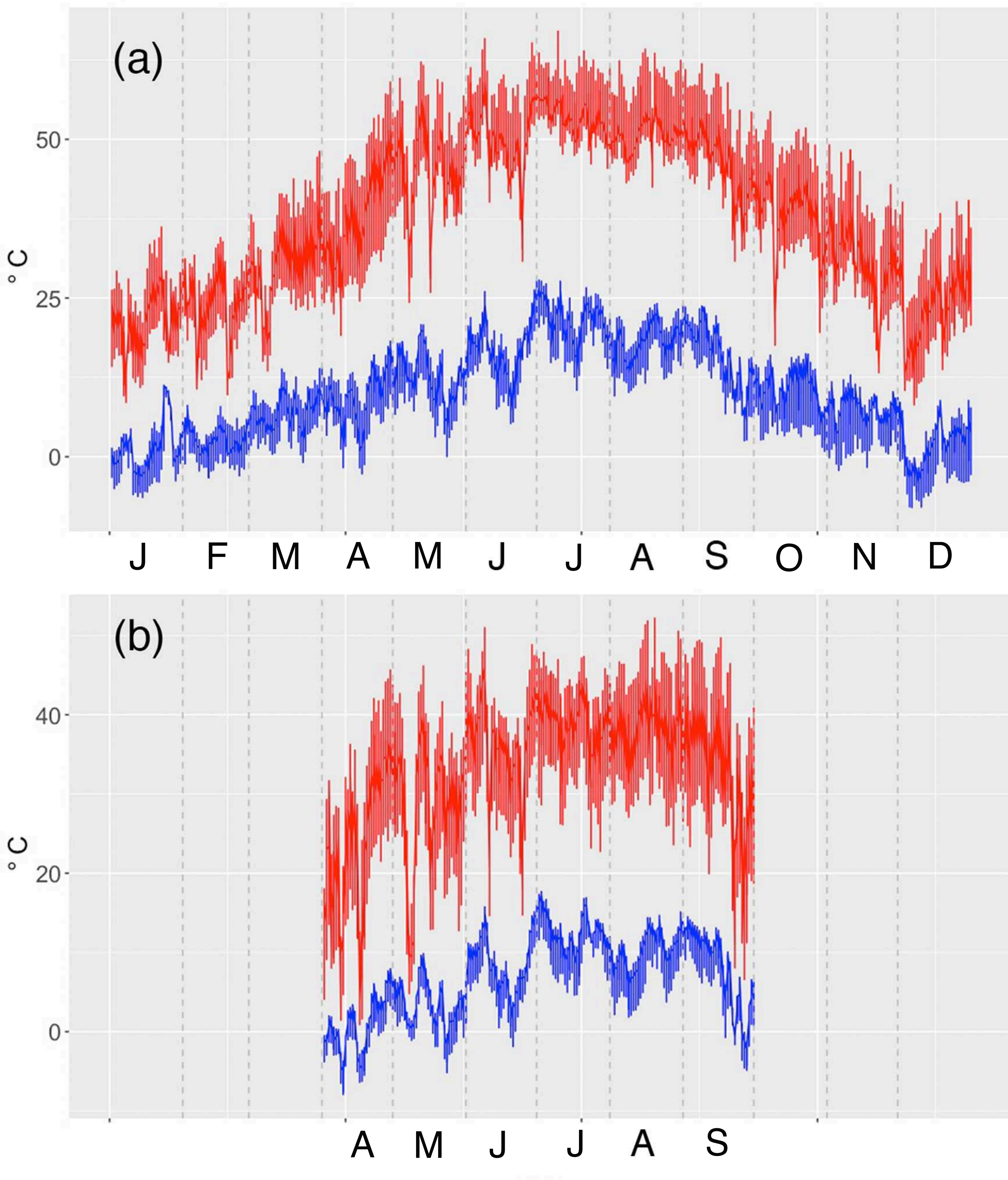

Figure 6

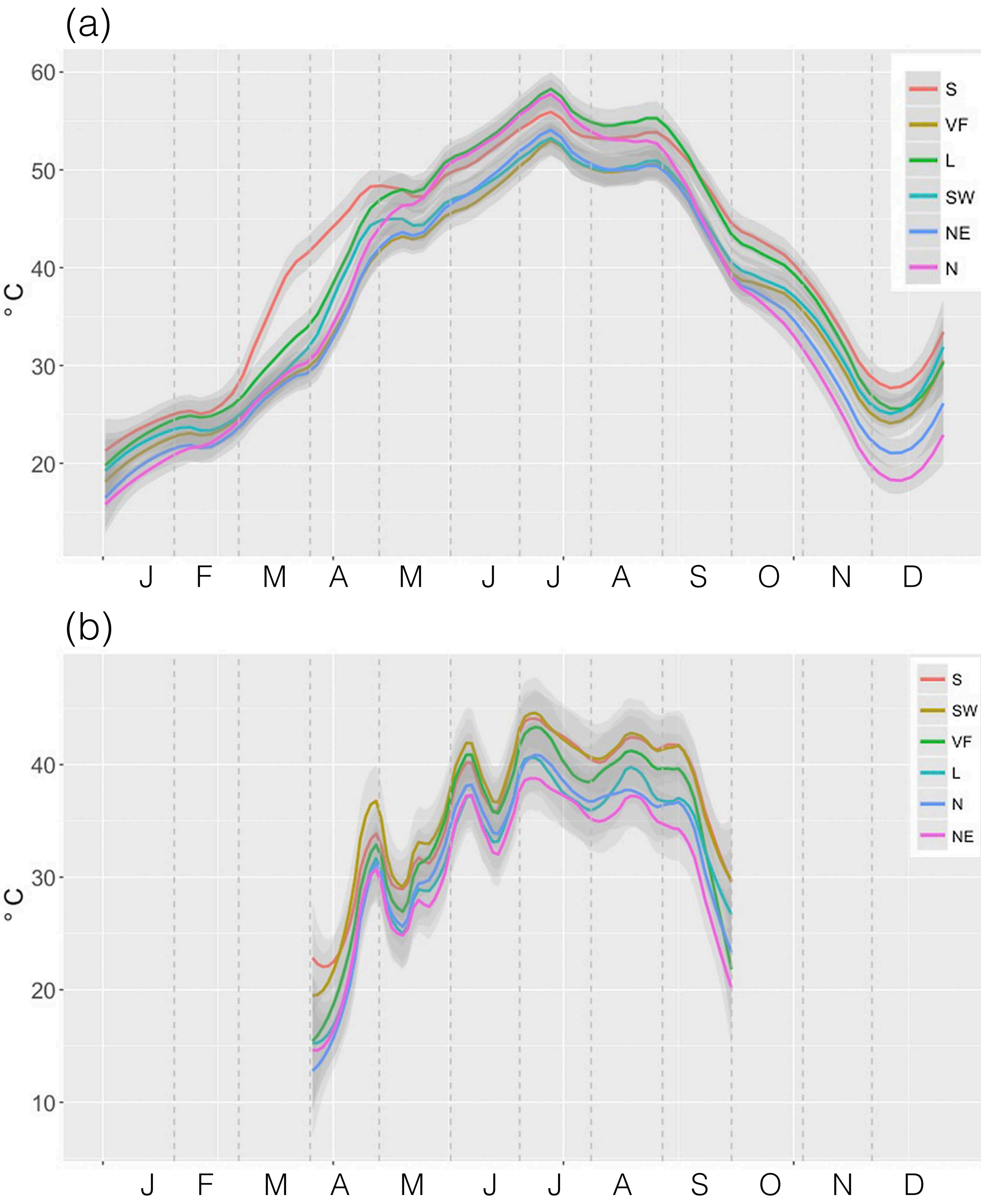
(a)
60
50
40
30
20
°C
S
VF
L
SW
NE
N
J
F
M
A
M
J
J
A
S
O
N
D
(b)
40
30
20
10
°C
S
SW
VF
L
N
NE
J
F
M
A
M
J
J
A
S
O
N
D

Figure 7

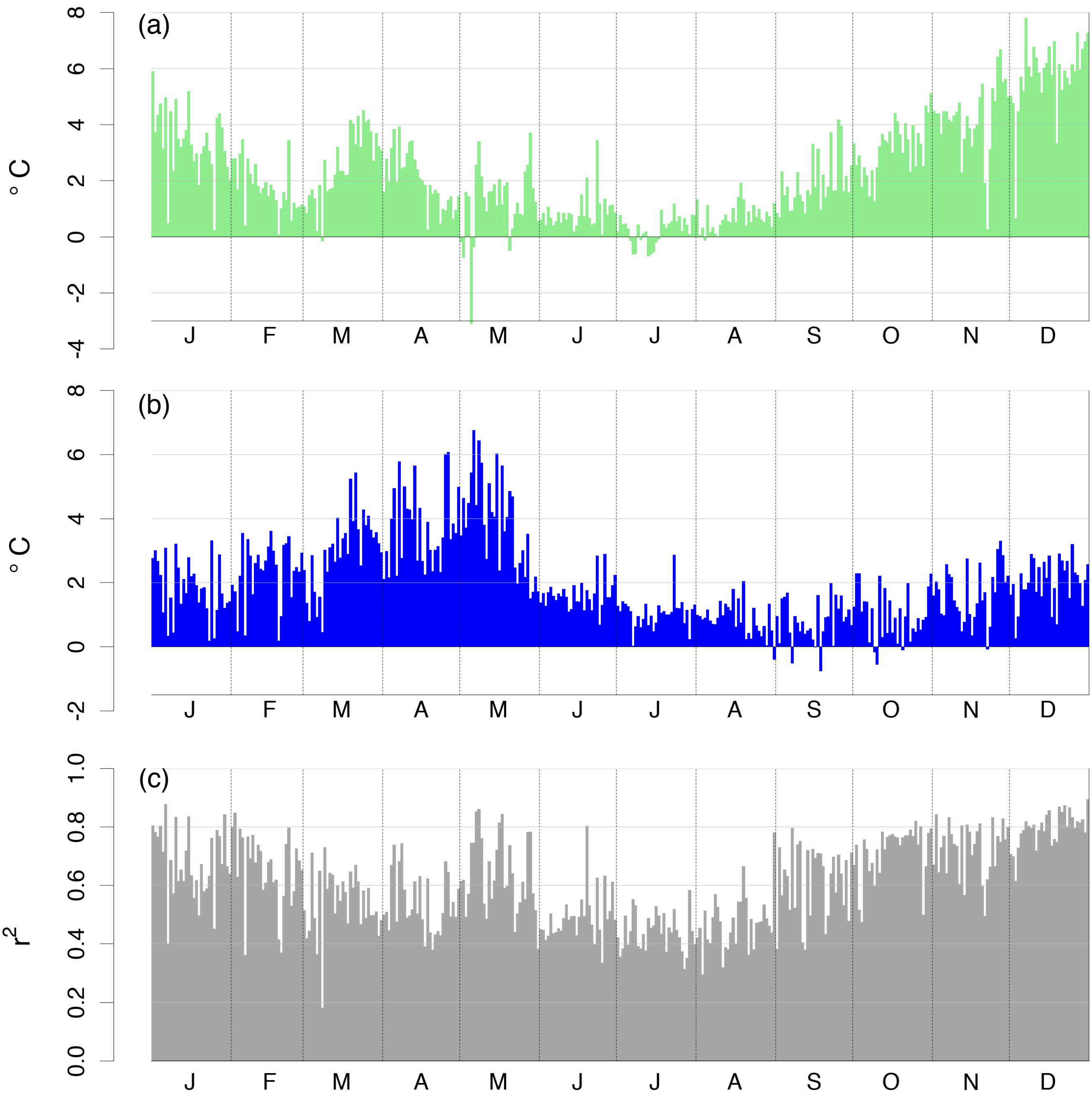
(a)
°C
8
6
4
2
0
-2
-4
J
F
M
A
M
J
J
A
S
O
N
D
(b)
°C
8
6
4
2
0
-2
J
F
M
A
M
J
J
A
S
O
N
D
(c)
r^2
1.0
0.8
0.6
0.4
0.2
0.0
J
F
M
A
M
J
J
A
S
O
N
D

Figure 8

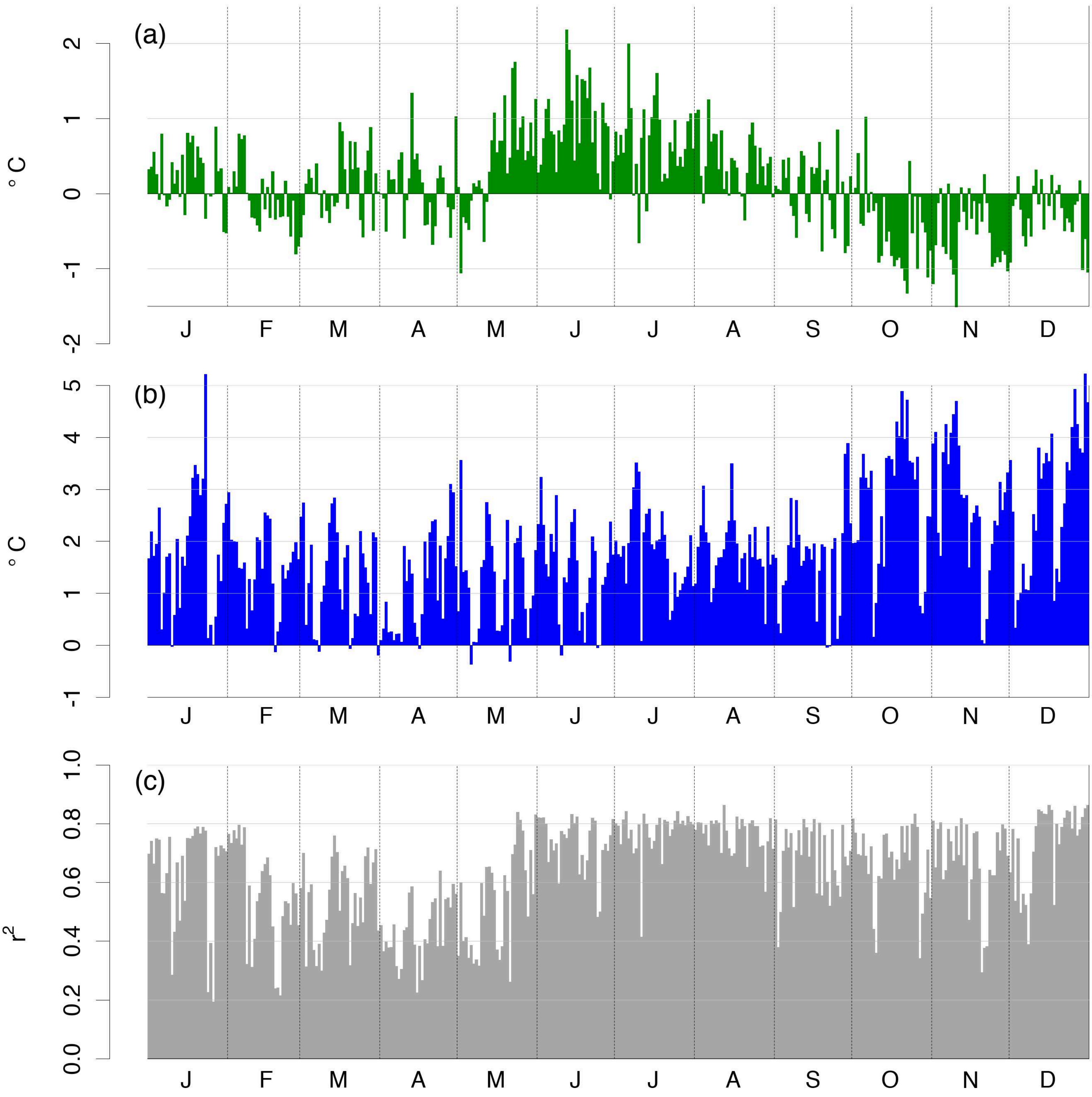

(a)
°C
2
1
0
-1
-2
J F M A M J J A S O N D
(b)
°C
5
4
3
2
1
0
-1
J F M A M J J A S O N D
(c)
r^2
1.0
0.8
0.6
0.4
0.2
0.0
J F M A M J J A S O N D

Figure 9

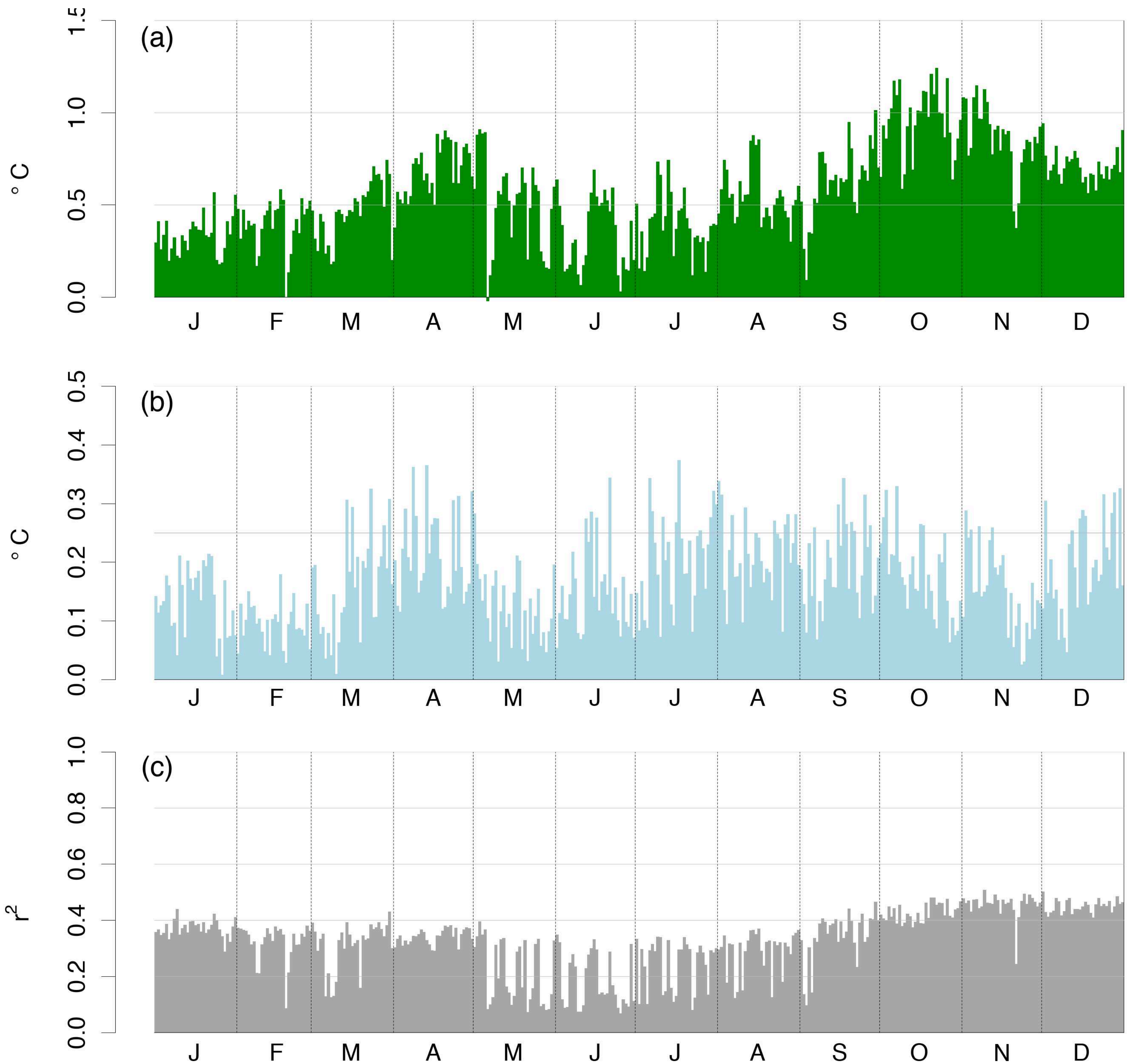
(a)
°C
0.0
0.5
1.0
1.5
J
F
M
A
M
J
J
A
S
O
N
D
(b)
°C
0.0
0.1
0.2
0.3
0.4
0.5
J
F
M
A
M
J
J
A
S
O
N
D
(c)
r^2
0.0
0.2
0.4
0.6
0.8
1.0
J
F
M
A
M
J
J
A
S
O
N
D

Figure 10

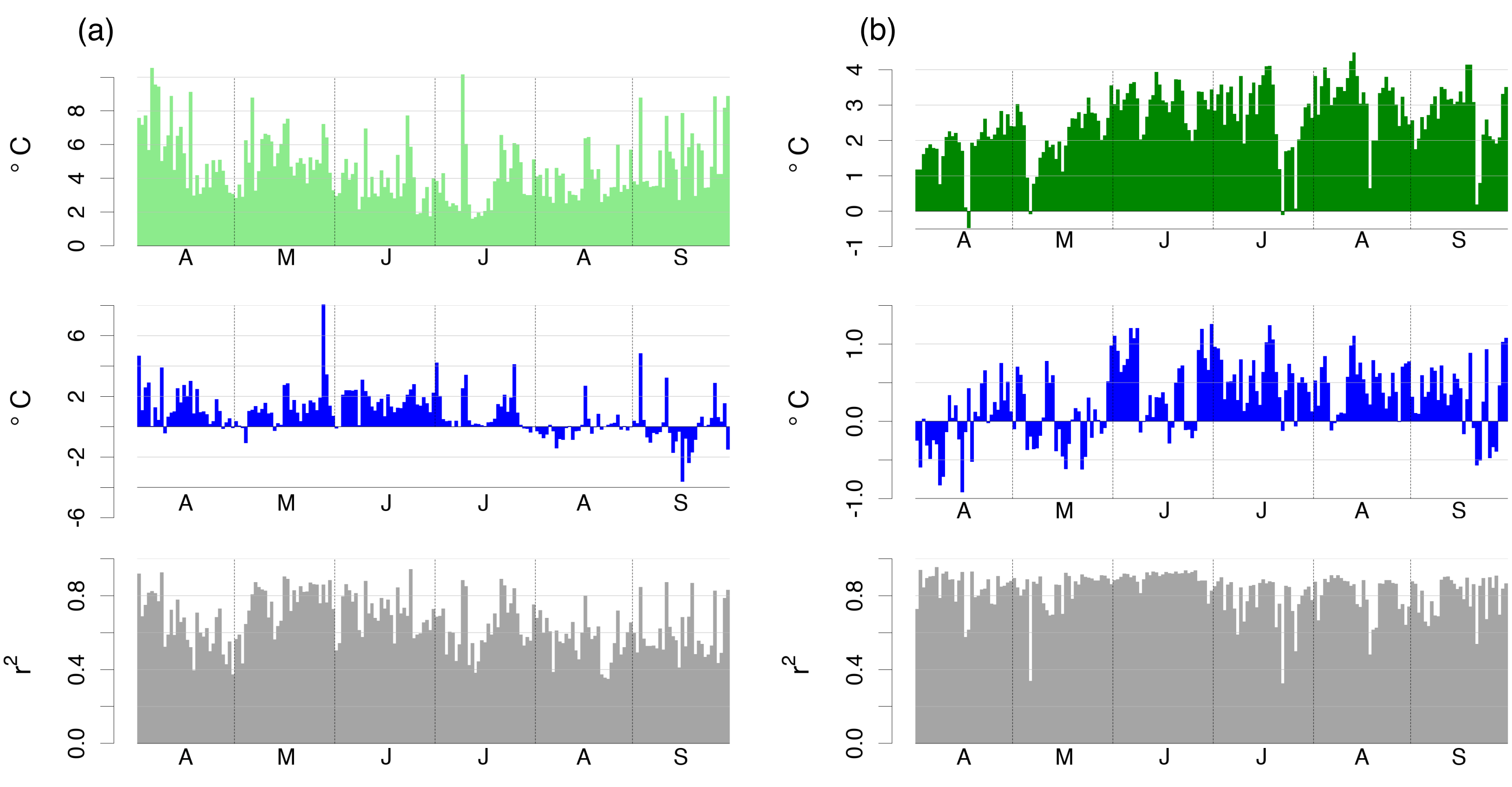

Figure A.1

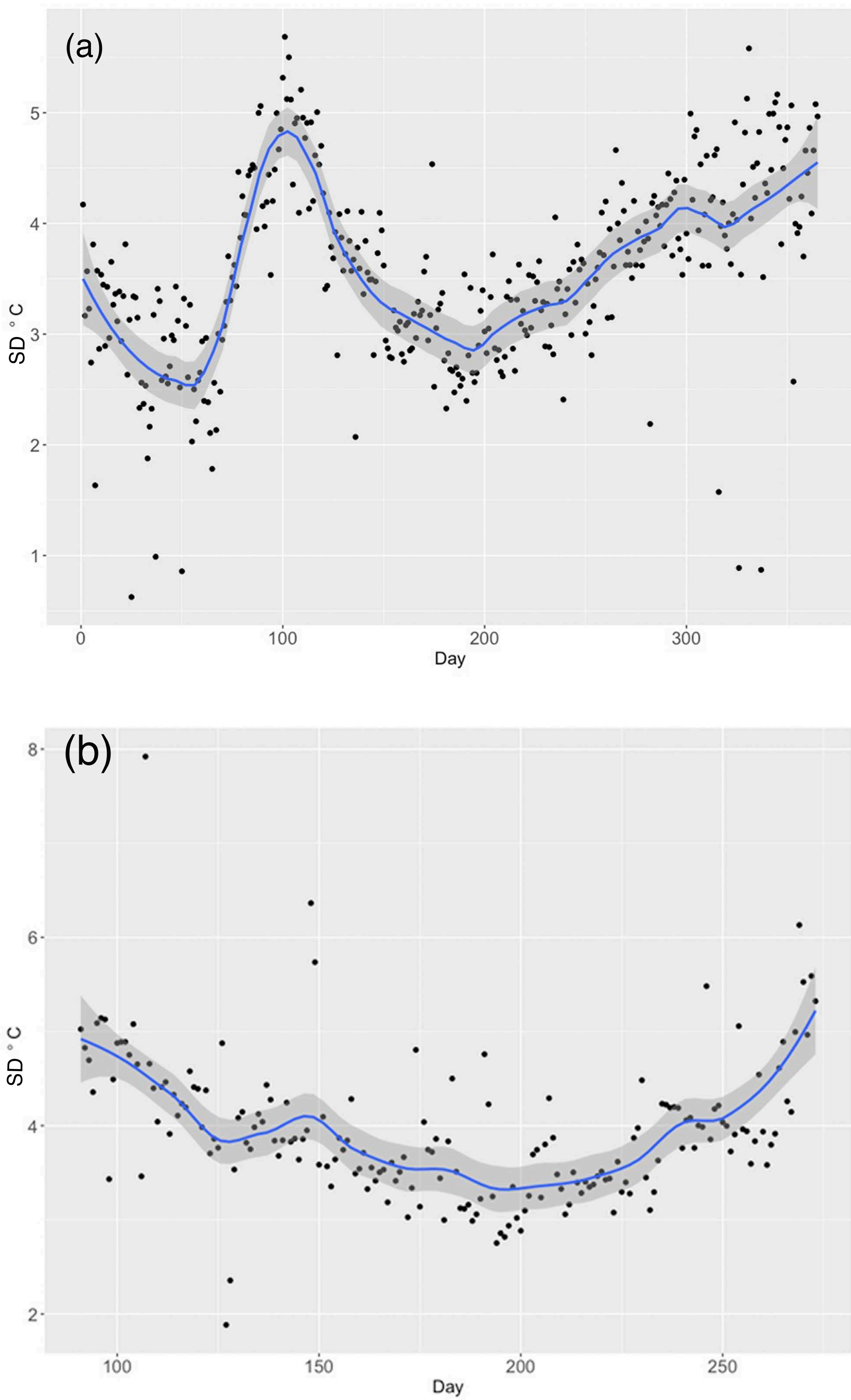

Figure A.2

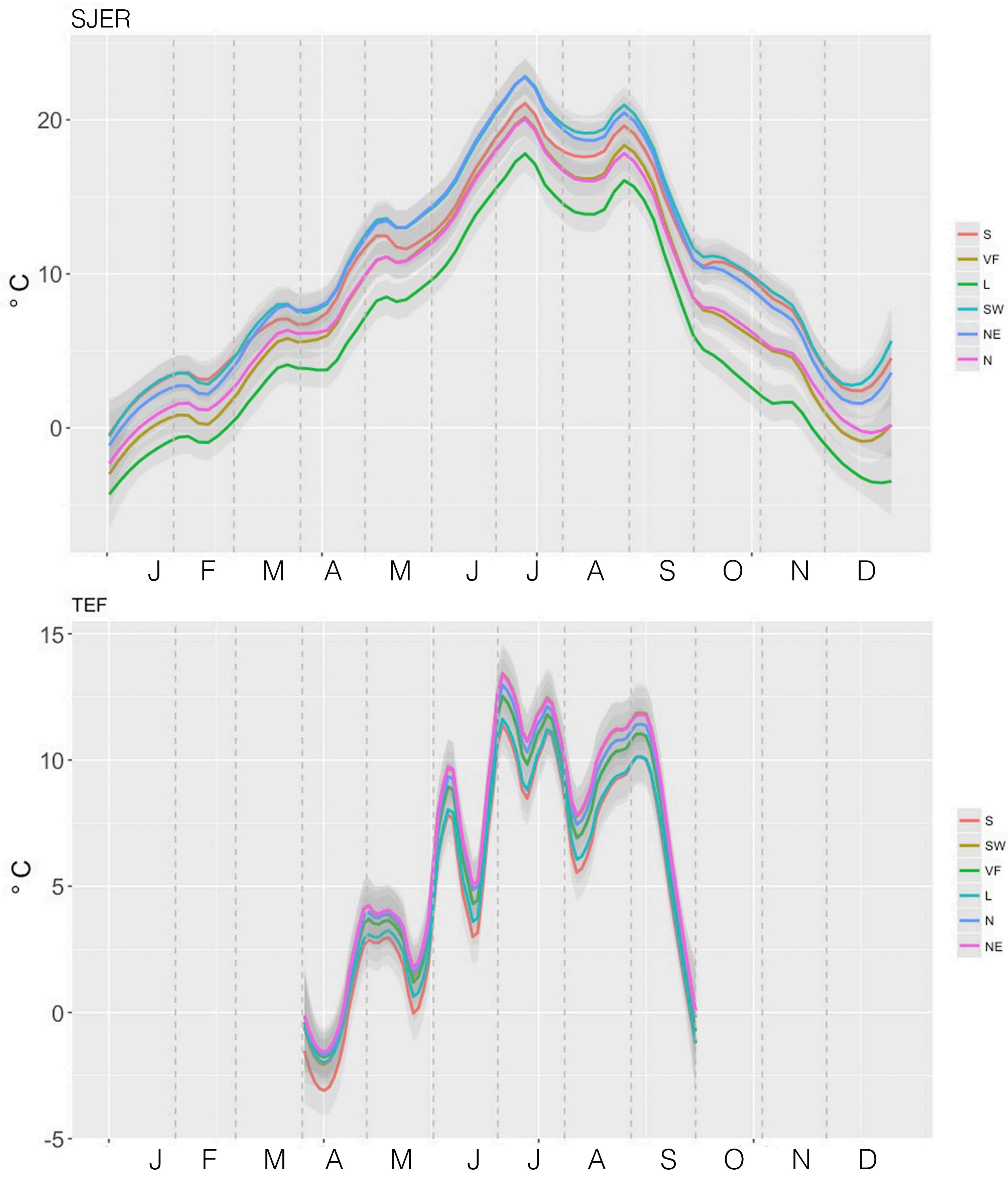

SJER
°C
20
10
0
J F M A M J J A S O N D
S
VF
L
SW
NE
N
TEF
°C
15
10
5
0
-5
J F M A M J J A S O N D
S
SW
VF
L
N
NE

Figure A.3

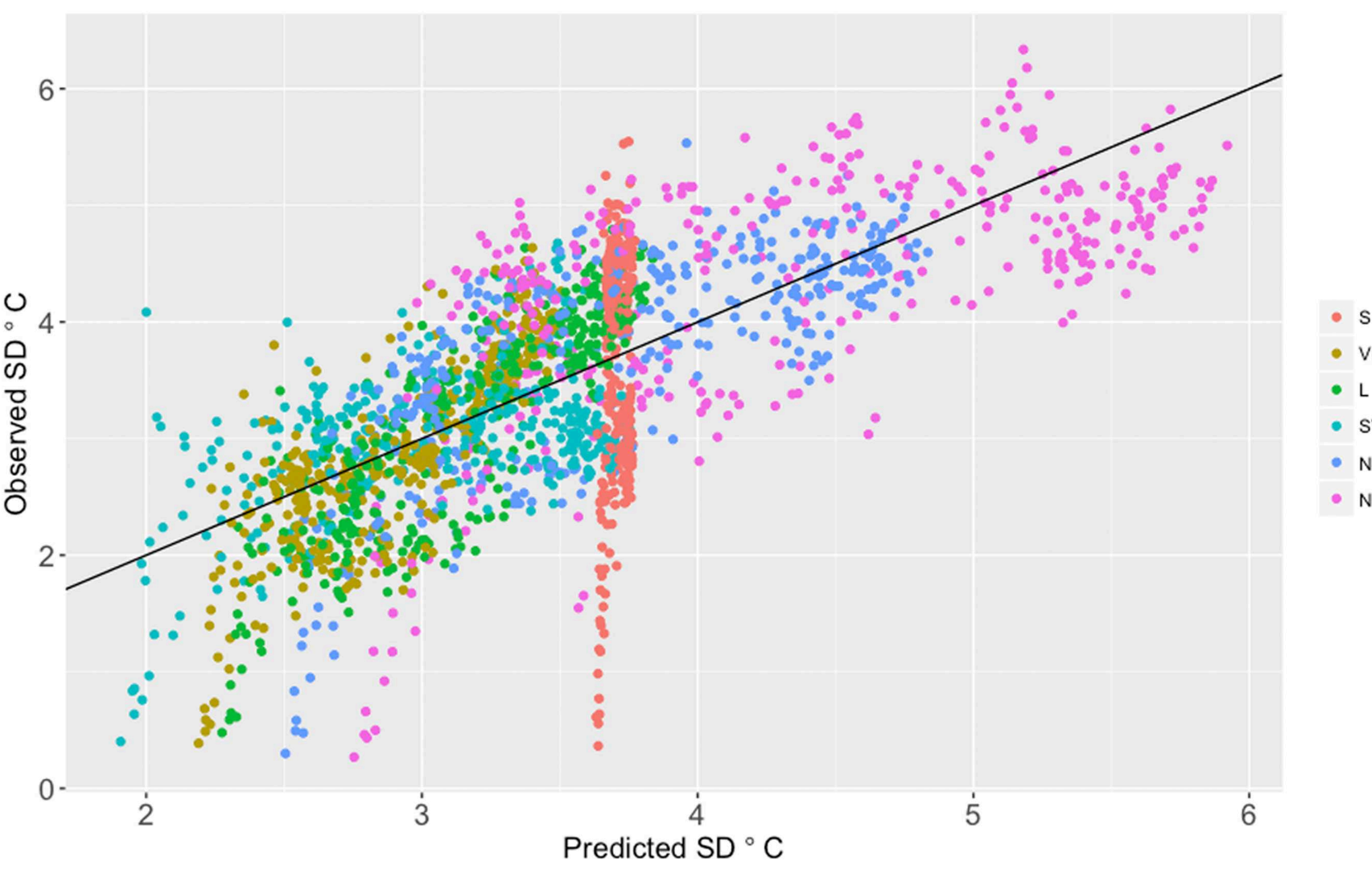

Figure A.4

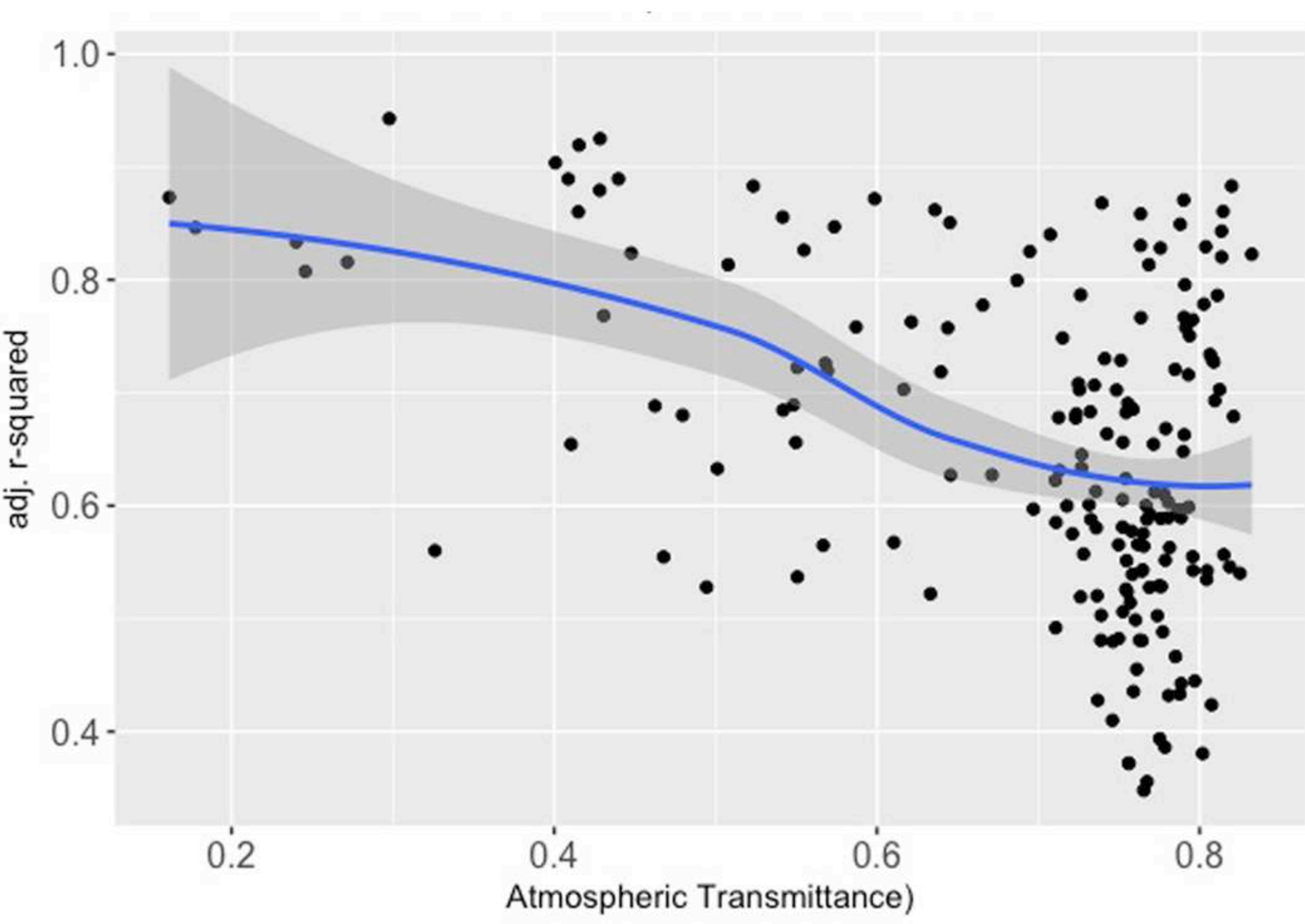
1.0
0.8
0.6
0.4
adj. r-squared
0.2
0.4
0.6
0.8
Atmospheric Transmittance)

Figure A.5

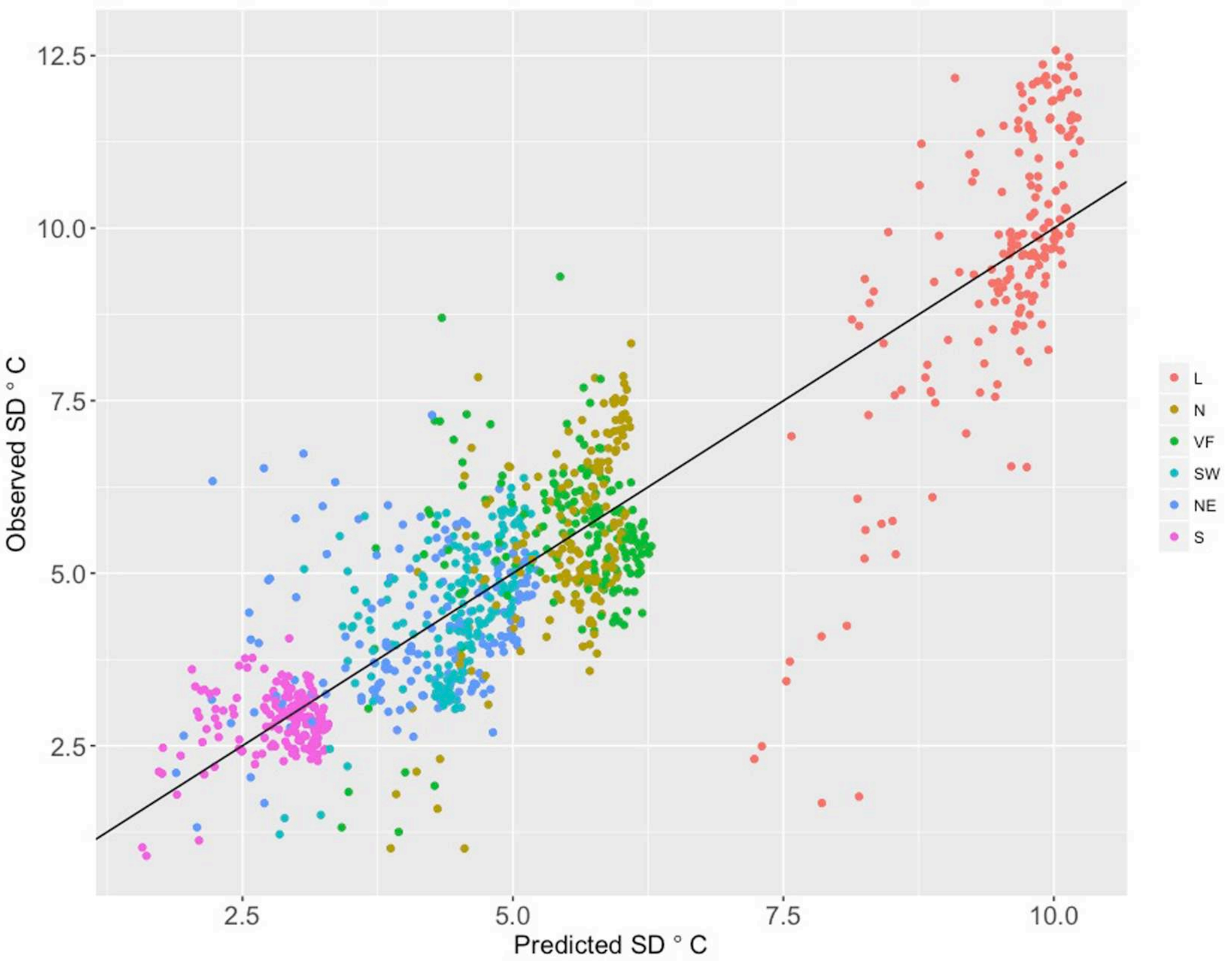
12.5
10.0
7.5
5.0
2.5
Observed SD ° C
2.5
5.0
7.5
10.0
Predicted SD ° C
L
N
VF
SW
NE
S